7-6-2005

A Theoretical Description of the Vibrational Sum Frequency Generation Spectroscopy of Interfaces

Angela S. Perry
University of South Florida

A Theoretical Description of the Vibrational Sum Frequency Generation Spectroscopy of Interfaces

by

Angela S. Perry

A dissertation submitted in partial fulfillment
of the requirements for the degree of
Doctor of Philosophy
Department of Chemistry
College of Arts and Sciences
University of South Florida

Major Professor: Brian Space, Ph.D.
Randy Larsen, Ph.D.
David Merkler, Ph.D.
David Rabson, Ph.D.

Date of Approval:
July 6, 2005

Keywords: water, molecular dynamics, liquid/vapor interface, nonlinear spectroscopy, SFG

Acknowledgments

First and foremost, I thank God for His countless blessings in my life and for the ability to succeed in this field.

I'd like to express my gratitude to my husband Mike, my parents, and my extended family whose love, support, and belief in me has been never ending. From the bottom of my heart, thank you.

I give my thanks and appreciation to Professor Brian Space, whose support and encouragement has been unwavering. His passion for science was inspiring and made this journey exciting.

Many thanks also to Professor Preston Moore, whose help and advice have been invaluable. I would also like to thank my committee: Dr. Randy Larsen, Dr. David Merkler, and Dr. David Rabson.

In addition, my sincere thanks goes out to my fellow group members: Christina Ridley, Ben Roney, Tony Green, Christine Neipert, Abe Stern, and especially Russell DeVane, who began this endeavor with me. I offer my thanks and appreciation for your support and friendship.

Note to Reader

Note to Reader: The original of this document contains color that is necessary for understanding the data. The original dissertation is on file with the USF library in Tampa, Florida.

Table of Contents

List of Figures

A Theoretical Description of the Vibrational Sum Frequency Generation Spectroscopy of Interfaces

Angela S. Perry

ABSTRACT

Our work investigates theoretical approximations to the interface specific sum frequency generation (SFG) spectra at aqueous interfaces constructed using time correlation function (TCF) and instantaneous normal mode (INM) methods. Both approaches lead to signals in excellent agreement with experimental measurements. This work demonstrates how TCF and INM methods can be used in a complementary fashion to describe interfacial vibrational spectroscopy.

Our approach is to compare TCF spectra with experiment to establish that our molecular dynamics (MD) methods can reliably describe the system of interest. We then employ INM methods to analyze the molecular and dynamical basis for the observed spectroscopy. We have been able to elucidate, on a molecularly detailed basis, a number of interfacial line shapes, most notably the origin of the complex O-H stretching SFG signal, and the identity of several intermolecular modes in the SFG spectra for the water/vapor interface. The success of both approaches suggests that theory can play a crucial role in interpreting SFG spectroscopy at more complex interfaces.

Chapter 1

Introduction

Liquid water interfaces are ubiquitous and important in chemistry and the environment. Thus, with the advent of interface specific nonlinear optical spectroscopies, such interfaces have been intensely studied – both theoretically [1–16] and experimentally. [17–44] SFG spectroscopy is a powerful experimental method for probing the structure and dynamics of interfaces. SFG is a second order polarization experiment, and the more common electronically nonresonant experiment is the focus of the work here. SFG spectroscopy is dipole forbidden in centrosymmetric media – such as liquids. Interfaces serve to break the isotropic symmetry, and produce a dipolar second order signal that is sensitive only to the interface in most cases. Contributions from bulk allowed quadrupolar effects have been demonstrated to be negligible in some cases, [45, 46] but can be included if necessary, [14] and, in that case, contributions from the bulk and interface are obtained in the sum frequency signal. The SFG experiment typically employs both a visible and infrared (IR) laser field overlapping in time and space at the interface, and can be performed in the time or frequency domain. [17, 23, 47–54] In the absence of any vibrational resonance at the instantaneous IR laser frequency, a structureless signal due to the static hyperpolarizability of the interface is obtained. [5, 20, 26] When the IR laser frequency is in tune with a vibration at the interface, a resonant lineshape is obtained with a characteristic shape that reflects both the structural and dynamical environment at the interface. [2, 15, 55]

Recent years have seen a great increase in the number of experimental groups performing SFG investigations. In contrast, molecularly detailed theoretical simulations of SFG spectra are comparatively few, and have only recently begun making a significant impact. Like all vibrational spectroscopies, the goal of SFG spectroscopy is to infer structural and dynamical properties from the observed spectroscopic signatures. In contrast to more traditional vibrational spectroscopies, SFG lineshapes tend to be more complex (reflecting the unique environment that is present at an interfacial boundary), and are not nearly as well understood. Thus, the advent of effective theoretical simulation techniques promises to help realize the potential of SFG spectroscopy to permit detailed characterization of interfaces on par with that done in the bulk. Further, in analogy with condensed phase experiments, SFG experiments have recently begun being performed using a variety of time and frequency domain techniques taking advantage of the flexibility inherent in measuring a second order polarization signal. [25, 56, 57]

Chapter 2 presents a general theory of nonlinear polarization, and specializing to second order processes. This formalism is needed to theoretically describe certain SFG experiments (especially time domain measurements) that do not utilize effectively monochromatic fields. Section 2.1 describes how the general formulas simplify in idealized limits – in which most extant experiments have been performed or interpreted. The expression derived there are those frequently presented in the SFG literature.

Next, relevant considerations concerning optical experiments at interfaces are presented including the origin and importance of Fresnel factors, and the phenomenological expression for the measured second order (SFG) intensity in terms of the signal field (Section 2.2). The relationship between the common experimental polarization conditions of the experimental fields (SSP, SPS, PPP, and PSS) and microscopic Cartesian

susceptibility tensor elements is also presented. The wave vector and phase matching conditions that need to be satisfied for coherent nonlinear optical experiments are discussed in Section 2.3.

Next, Section 2.4 presents formal expressions for dipolar contributions to the sum frequency signal. The microscopic formulas for the dipolar SFG susceptibility tensor are also presented along with a discussion of the rotating wave approximation in this context. These expressions provide the tie between the earlier phenomenological expression, and the formulas needed to relate a system's dynamics to an SFG signal.

Chapters 3 and 4 contain the theoretical background for the TCF and INM methods, respectively. Section 3.2 discusses the time domain approach to calculating SFG spectra. Section 4.2 presents a frequency domain approach to calculating SFG signals. Chapter 5 presents the polarizability model used throughout this work.

Chapter 6 discusses theoretical simulations and their results with a focus on the water/vapor interface; comparison with experiment is stressed. Results, including the identification of novel species at the water/vapor interface, are presented. Chapter 7 presents conclusions, and a brief discussion of future directions for theoretical studies of SFG spectroscopy.

Chapter 2

Theoretical Background of Nonlinear Polarization

SFG experiments measure a second-order polarization generated coherently in a direction given by the experimental wave vector and phase-matching conditions. [25, 56, 58] It is one of several second-order processes that are possible when two electric fields interact with a medium. The focus of this work is on SFG experiments, although some of the formalism presented is more general. Such measurements are interface specific because even-order polarization generating terms are forbidden in centrosymmetric media. This can be understood by considering reversing the direction of all the electric fields in an experiment for an isotropic system. Doing so must change the sign of the polarization because all directions are equivalent on average. [58] However, even numbers of fields will make the polarization equal to its negative – a condition that insists the polarization is zero, *i.e.* $\mathbf{P} = -\mathbf{P} = 0$. [56] At an interface, or in certain noncentrosymmetric solids, [25] the isotropy of the system is broken. This leads to a second-order signal within the dipole approximation, and in this case, the signal is proportional to the product of the susceptibility and the electric fields as described below.

It should also be noted, even in centrosymmetric media, bulk quadrupolar contribu-

tions to SFG signals are possible, but have been shown to be negligible in most cases involving liquid interfaces in the common SFG reflected geometry. [45, 46, 54, 59] (When light impinges on an interface, a SFG signal is generated. This signal is both reflected from the boundary, and transmitted through the interface.) [60] They can, however, be important for experiments performed in the transmission geometry. [46] In the case of bulk quadrupoles, their contribution to the second-order signal is proportional to derivatives of the field which invalidates the above symmetry argument.

Like all nonlinear optical experiments, both time and frequency domain approaches to SFG are possible. [47, 56] To date, most SFG experiments have been performed in the frequency domain, and, effectively, in the limit of monochromatic fields. [17, 23, 51–54] However, there is growing interest in using both time-domain, mixed time and frequency domain approaches, [47–50] and also looking at other second-order processes such as difference frequency generation (DFG) spectroscopy. [61–64] The theoretical methods discussed below are capable of describing any of these second-order processes. Thus, before specializing the theoretical expressions to the typical monochromatic frequency domain experiment, it is helpful to examine the formal theoretical structure of second-order nonlinear processes. The resulting expressions will be required in calculating signals from experiments outside of the frequency-monochromatic or time-impulsive limit, *e.g.* typical time-domain experiments. Such experiments are becoming increasingly common because they can provide, in principle, information distinct from ideal frequency-domain experiments. [48]

First, considering an N^{th} order process (an $N+1$ wave-mixing experiment), an electric

field is applied at time t at position $\mathbf{r}$, and can be written:

$$\mathbf{E}(\mathbf{r},t) = \sum_{n}^{N} \left(\mathbf{E}_n(\mathbf{t}) e^{i\mathbf{k_n}\cdot\mathbf{r}} + \mathbf{E}_n^*(\mathbf{t}) e^{-i\mathbf{k_n}\cdot\mathbf{r}} \right) \tag{2.1}$$

In Equation 2.1, $\mathbf{k_n}$ is the wave vector specifying the field-propagation direction. Equation 2.1 is partitioned into components that are slowly varying in space, and those that are spatially highly oscillatory. [25, 56, 65] The slowly varying spatial component, $\mathbf{E_n}(t)$, can generally be further decomposed into temporally ($\epsilon_n(t)$) and spatially ($\mathbf{E}_n$) dependent parts. [65] This subsequent separation allows the field to be rewritten in the form:

$$\mathbf{E}(\mathbf{r},t) = \sum_{n}^{N} \left(\mathbf{E}_n \epsilon_n(t) e^{i\mathbf{k_n}\cdot\mathbf{r}} + \mathbf{E}_n^* \epsilon_n^*(t) e^{-i\mathbf{k_n}\cdot\mathbf{r}} \right) \tag{2.2}$$

In Equations 2.1 and 2.2, the sum on n is included because, in the most general case, exact time ordering of the applied fields cannot be assumed. [56] In practice, experiments in the time domain typically use relatively short pulses that are separated and ordered in time while the frequency domain techniques employ nearly monochromatic laser fields that overlap in time and space – such considerations simplify the required analysis considerably.

Given the field, the observable nonlinear polarization, $\mathbf{P}^{(N)}$, (within the dipole approximation where the response function and susceptibility tensors are independent of $\mathbf{r}$ and $\mathbf{k}$) takes the form of a multiple time integration over the material response function, $\mathbf{R}^{(N)}$, which contains all the system variables and information to be probed. (The material system in the time domain is described by the response function, and is typically referred to as the susceptibility in the frequency domain.)

$$\mathbf{P}^{(N)}(\mathbf{r},t) = \int_0^\infty d\tau_1 \cdots \int_0^\infty d\tau_N \; \mathbf{R}^{(N)}(\tau_1, \cdots, \tau_N) \mid \mathbf{E}(\mathbf{r}, t-\tau_1) \cdots \mathbf{E}(\mathbf{r}, t-\tau_N) \tag{2.3}$$

In Equation 2.3, the vertical line represents N tensor contractions. In an N order experiment, there are N relevant times – corresponding to the number of $\mathbf{E}(\mathbf{r},t)$'s in the expression for $\mathbf{P}^{(N)}(\mathbf{r},t)$ that are each represented by the sum in Equations 2.1 or 2.2. Consequently, when exact time ordering of the applied fields cannot be assumed, and Equation 2.1 is used to describe the applied fields, a sum of $(2N)^N$ terms determine the N^{th} order polarization. The polarization can then be written as:

$$\mathbf{P}^{(N)}(\mathbf{r},t) = \sum_{s}^{2^N N^N} \mathbf{P}^{(N)}(\mathbf{k_s},t) = \sum_{s}^{2^N N^N} \mathbf{P}^{(N)}(t) e^{i\mathbf{k_s}\cdot\mathbf{r}} \tag{2.4}$$

In Equation 2.4, $\mathbf{k_s}$ is the sum of the wave vectors associated with the applied fields and represents the direction in which the generated signal will propagate. As is shown in Figure 2.1, considering a second-order experiment probing an interface, after the nonlinear signal is generated, it will interact with the interface producing a reflected and transmitted signal with modified wave vectors (this issue will be discussed in Section 2.3). Note, $\mathbf{P}^{(N)}(\mathbf{k_s},t)$ is a complex quantity, and it is *one* of the $(2N)^N$ processes that determines the total N^{th} order polarization, $\mathbf{P}^{(N)}(\mathbf{r},t)$. Further, $\mathbf{P}^{(N)}(\mathbf{r},t)$ is a real quantity, and is the sum of all the $\mathbf{P}^{(N)}(\mathbf{k_s},t)$ terms (Equation 2.4). However, once a particular $\mathbf{k_s}$ is chosen (*e.g.*, by the experimental geometry) the signal is a complex quantity, and the real and imaginary parts can be measured separately – *e.g.*, in a heterodyne detected experiment. [66]

In principle, the sum of all $(2N)^N$ terms must be evaluated to calculate the total N^{th} order polarization. Considering second order experiments, this leads to 16 distinct contributions. In practice, the polarization generated for a given experiment is associated with a particular wave vector and phase-matching condition. This implies when the two

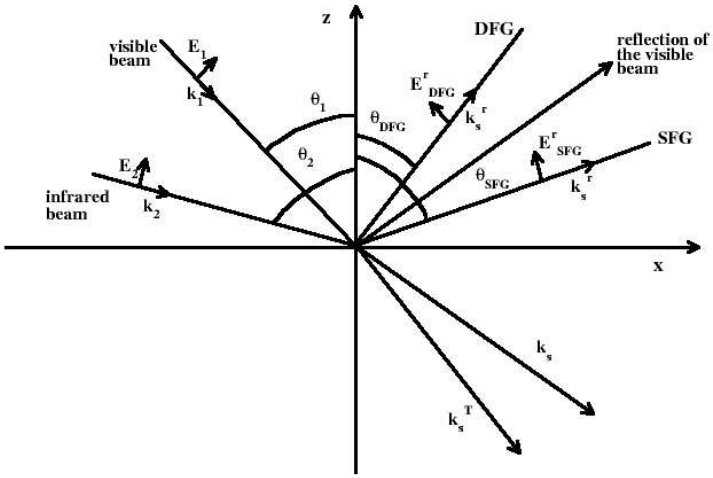

Figure 2.1: Coplanar Geometry of the Beams. Coplanar geometry of the incident, reflected and transmitted beams. θ_1 (θ_2) is the angle of incidence with respect to the z-axis of the visible (IR) field. θ_{SFG} (θ_{DFG}) is the angle the generated SFG (DFG) signal is radiated at. $\mathbf{k}_1$ ($\mathbf{k}_2$) is the wave vector of the visible (IR) field. $\mathbf{k}_s{}^r$ ($\mathbf{k}_s{}^T$) is the wave vector of the reflected (transmitted) field, and $\mathbf{k}_s = \mathbf{k}_1 + \mathbf{k}_2$. All incident fields are assumed to lie in the same xz plane which is normal to the surface.

incident wave vectors add, a SFG signal is generated, and when the two incident wave vectors interact such that the resulting wave vector is equal to their difference, a DFG signal is generated. For surface probing spectroscopies, the direction the signal (DFG and/or SFG) propagates in will be guided by Snell's (linear and nonlinear) refraction and reflection laws in conjunction with the original propagation directions of incident wave vectors, $\mathbf{k_1}$ and $\mathbf{k_2}$. Thus, with the proper experimental setup in which detectors

are placed at the appropriate phase matched angle, it is typical to only detect one of the possible second-order nonlinear processes, *e.g.* SFG or DFG. Phase-matching criteria for surface probing spectroscopies will be discussed more throughly in Section 2.3.

In a similar manner, in formulating theoretical descriptions of the response function, $\mathbf{R}^{(2)}$, a given experiment may only be sensitive to a part of the response, and it is convenient to discard portions that do not contribute significantly. [61] This is accomplished by identifying terms in the response function that oscillate in time so as to phase cancel with those from the applied fields, and subsequently discarding the remaining terms. This is called the rotating wave approximation (RWA). Computationally, this approximation allows for inclusion of only fully resonant Louiville space pathways and depends implicitly on the reference or model system being considered. [56, 61, 65] The RWA is a computational convenience; it is possible to include the entire response function, and perform the integration in Equation 2.3 (or presented specifically for second-order processes such as SFG in Equation 2.5 below) explicitly. [67]

Note, a particular experiment measures either the modulus of the complex $\mathbf{P}^{(N)}(\mathbf{k_s}, t)$ (homodyne detection) or its real or imaginary parts (heterodyne detection). [66,68] Methods using interference effects (*via* homodyne detection) between bulk and interfacial contributions to an SFG signal have also been used to separately measure the real and imaginary contributions at aqueous quartz interfaces. [17, 69] The real and imaginary parts of the response contain information that is not obtainable *via* measuring the modulus of the signal. [3, 17] The limits of ideal frequency and impulsive fields will simplify the calculation of the polarization as will be shown in the following section.

2.1 Calculating the Polarization in Limiting Cases – Monochromatic and Impulsive Light

The second-order time dependent polarization is defined by [25, 56, 58, 70, 71]

$$\mathbf{P}^{(2)}(\mathbf{k_s}, t) = e^{i\mathbf{k_s}\cdot\mathbf{r}} \int_0^\infty d\tau_1 \int_0^\infty d\tau_2 \; \mathbf{R}^{(2)}(\tau_1, \tau_2) : \mathbf{E}_1(t-\tau_1)\mathbf{E_2}(t-\tau_2) \tag{2.5}$$

In Equation 2.5, $\mathbf{R}^{(2)}(\tau_1,\tau_2)$ is the system's second-order response function (a real quantity), τ_1 and τ_2 represent time delays between the first and second fields, and the second field and time of signal detection respectively. Note, the symbol ":" denotes contraction of the two dimensional tensor (response or susceptibility) with the fields. A direct relationship between this quantity and the second-order frequency-dependent susceptibility can be established by representing the time-dependent components of the applied fields as their Fourier transform:

$$\mathbf{P}^{(2)}(\mathbf{k_s}, t) = \frac{e^{i\mathbf{k_s}\cdot\mathbf{r}}}{4\pi^2} \int_{-\infty}^\infty d\omega_1 \int_{-\infty}^\infty d\omega_2 \int_0^\infty d\tau_1 \int_0^\infty d\tau_2 \mathbf{R}^{(2)}(\tau_1, \tau_2) : \mathbf{E}_1(\omega_1)\mathbf{E}_2(\omega_2) e^{-i\omega_1(t-\tau_1)-i\omega_2(t-\tau_2)} \tag{2.6}$$

The double Fourier-Laplace transform of the system's response function is now identified as the second-order susceptibility, $\boldsymbol{\chi}$: [56, 70]

$$\boldsymbol{\chi}^{(2)}(\omega_1, \omega_2) = \int_0^\infty d\tau_1 \int_0^\infty d\tau_2 \; \mathbf{R}^{(2)}(\tau_1, \tau_2) \; e^{i\omega_1\tau_1} e^{i\omega_2\tau_2} \tag{2.7}$$

Because the susceptibility results from a Fourier-Laplace transform of the (real) response function, it is a complex quantity (the Fourier transform of the response function is, however, a real function). Substitution of Equation 2.7 into Equation 2.6 gives the time-dependent polarization in terms of the back Fourier transform of the product of the

frequency domain fields and susceptibility:

$$\mathbf{P}^{(2)}(\mathbf{k_s},t) = \frac{e^{i\mathbf{k_s}\cdot\mathbf{r}}}{(2\pi)^2}\int_{-\infty}^{\infty} d\omega_1 \int_{-\infty}^{\infty} d\omega_2 \; \boldsymbol{\chi}^{(2)}(\omega_1,\omega_2){:}\mathbf{E}_1(\omega_1)\mathbf{E}_2(\omega_2)\; e^{-it(\omega_1+\omega_2)} \tag{2.8}$$

Fourier transforming the polarization with respect to time gives the frequency dependent polarization where the signal frequency, Ω_s, is the transform variable conjugate to t, and $\omega_s = \omega_1 + \omega_2$:

$$\mathbf{P}^{(2)}(\mathbf{k_s},\Omega_s) = \frac{e^{i\mathbf{k_s}\cdot\mathbf{r}}}{(2\pi)^2}\int_{-\infty}^{\infty} d\omega_1 \int_{-\infty}^{\infty} d\omega_2 \; \boldsymbol{\chi}^{(2)}(\omega_1,\omega_2){:}\mathbf{E}_1(\omega_1)\mathbf{E}_2(\omega_2)\int_{-\infty}^{\infty} dt\; e^{-it(\omega_s-\Omega_s)} \tag{2.9}$$

$$\mathbf{P}^{(2)}(\mathbf{k_s},\Omega_s) = \frac{e^{i\mathbf{k_s}\cdot\mathbf{r}}}{2\pi}\int_{-\infty}^{\infty} d\omega_1 \int_{-\infty}^{\infty} d\omega_2 \; \delta(\omega_s-\Omega_s)\boldsymbol{\chi}^{(2)}(\omega_1,\omega_2){:}\mathbf{E}_1(\omega_1)\mathbf{E}_2(\omega_2) \tag{2.10}$$

Unlike Equation 2.7, causality does not require a Fourier-Laplace transform because no system function is directly involved in the transform. Integration of the complex exponential over t, the time of signal detection, results in the delta function in Equation 2.10. In the limit the applied fields are monochromatic (the limit in which most frequency domain SFG experiments are performed), they may be represented as complex exponentials in the time domain and will be delta functions in the frequency domain: $\mathbf{E}(\omega_i) = 2\pi\mathbf{E}_i\delta(\omega_i - \Omega_i)$. Thus, an ideal-frequency domain experiment directly probes the susceptibility:

$$\mathbf{P}^{(2)}(\mathbf{k_s},\Omega_s) = 2\pi e^{i\mathbf{k_s}\cdot\mathbf{r}}\boldsymbol{\chi}^{(2)}(\Omega_1,\Omega_2){:}\mathbf{E}_1\mathbf{E}_2\delta(\omega_s-\Omega_s) \tag{2.11}$$

Note, as a result of the form of $\boldsymbol{\chi}$, $\Omega_s = \Omega_1 + \Omega_2$ is the signal frequency, and is at the sum of the input frequencies; $\boldsymbol{\chi}$ is described in Section 2.4. In an SFG experiment, both frequencies would be positive, and a sum frequency detected. In a DFG experiment, one

of the input frequencies would have a negative sign associated with it, and a difference frequency would be generated.

The limit of ideal frequency (monochromatic applied fields) is just one common means of simplifying the integrals necessary to calculate the second-order polarization. The opposite limit, the impulsive limit, occurs when the fastest material timescale is much longer than the durations of the applied fields. This limit is often assumed in theoretical developments for simplification purposes, but generally is not truly justifiable – temporal pulse durations are not currently faster than even the shortest vibrational time scale. [56] In this limit, the applied field's temporal envelopes behave as delta functions - making the evaluation of Equation 2.5 trivial. The resulting expression for an impulsive field at some time $\tilde{\tau}$ is

$$\mathbf{E}_i(\tau') = \mathbf{E}_i \delta(\tau' - \tilde{\tau}) e^{-i\omega_i \tilde{\tau}} \tag{2.12}$$

$$\mathbf{P}^{(2)}(\mathbf{k_s}, t) = e^{i\mathbf{k_s}\cdot\mathbf{r}} \mathbf{R}^{(2)}(t - \tilde{\tau}_1, t - \tilde{\tau}_2) : \mathbf{E}_1 \mathbf{E}_2 e^{-i(\omega_1 \tilde{\tau}_1 + \omega_2 \tilde{\tau}_2)} \tag{2.13}$$

Note, the applied fields in Equation 2.12 can also have an exponential phase factor associated with them. [72] While Equation 2.12 implies the experiment probes the entire response function, finite, yet short, pulses (that do not have the infinite frequency spectrum that a delta function pulse would contain) are only resonant with certain parts of the response function. To correct for this deficiency, it is useful to write the response function in terms of Louiville space pathways. [56] In this language, one should only include fully resonant Louiville space pathways of the susceptibility (response) tensor in the polarization calculation – this is equivalent to invoking the RWA. [56, 65, 73] In

practice, this limit is commonly assumed for simplicity in calculating the polarization; it makes evaluation of the integrals in Equation 2.5 trivial. In this case, it is *necessary* to include only pathways that are expected to contribute for a given set of fields and a relevant model system. [56, 72]

2.2 The Measured Intensity Including Dielectric Effects from the Interfacial Boundaries

Because interfaces necessarily include dielectric boundaries, the equations derived thus far need to be modified accordingly – the measured signal will include factors due to interactions with the boundaries. [74–76] The fields in the above derivations are local to the medium, and SFG excitation fields must travel through the vacuum before overlapping at the interface (for liquid/vapor or gas/solid interfaces) or through some other medium when considering a buried interface. When the fields combine at the interface, a second-order nonlinear signal is produced that interacts with the dielectric boundaries. Hence, the observed fields must be related to the laboratory-generated fields through Fresnel coefficients. [25, 60] In a boundless medium, the Fresnel coefficients reduce to unity, and the laboratory and local fields are the same. [74]

Experimentally, it is the intensity generated at the sum frequency of the two input beams that is measured (in typical homodyne detection experiments). Equation 2.14 [25, 46, 70, 74, 77] describes the relationship between the field, $\mathbf{E}(\mathbf{r}, \omega_s)$, and the measured intensity, $I(\omega_s)$, generated at the sum frequency of the two input fields:

$$I(\omega_s) = \frac{c\sqrt{\epsilon_1(\omega_s)}|\mathbf{E}(\mathbf{r}, \omega_s)|^2}{2\pi} \tag{2.14}$$

$\mathbf{E}(\mathbf{r}, \omega_s)$ is found through the use of (nonlinear) Maxwell's wave equation – knowing the nonlinear polarization one can solve for the field. [25, 78, 79] The exact form of the relationship between the nonlinear polarization and the measured intensity generally depends on the boundary conditions of the medium, the direction $\mathbf{E}(\mathbf{r}, \omega_s)$ propagates in, how well phase-matching can be achieved, whether or not the slowly-varying-envelope approximation is made, and the form of the applied fields – i.e, monochromatic, Gaussian, etc. In general, the local fields are approximated as monochromatic, and the slowly-varying-envelope approximation is assumed to be valid. Explicit expressions using various approximations are available in the literature. [25, 46, 60, 74] Generally, the intensity is found to be proportional to the square of the sum frequency multiplied by the amplitude of the nonlinear polarization:

$$I(\omega_s) \propto \omega_s^2 |\mathbf{P}(\omega_s) e^{i\mathbf{k_s}\cdot\mathbf{r}}|^2 \tag{2.15}$$

The proportionality coefficients include the Fresnel factors that are typically calculated using an appropriate model of the experimental setup. [15] In order to compare directly theoretical and experimental spectra, it is necessary to include the Fresnel factors – especially when comparing relative intensities from different polarization conditions. [2, 15]

As demonstrated in Section 2.1, in the limit of monochromatic fields, the polarization directly probes the susceptibility (Equation 2.11). Following from Equation 2.15, in this limit, the measured intensity will also directly probe the (the squared modulus of the) susceptibility tensor of the system. In total, the surface susceptibility tensor contains 27 elements. Consideration of symmetry conditions for a typical azimuthally isotropic

interface requires all but 7 elements of the susceptibility tensor to vanish because the elements need to be invariant with respect to symmetry operations that preserve the (azimuthal) symmetry. [63] Additionally, of the 7 nonvanishing components, only four are, in general, unique ($\chi_{xzx} = \chi_{yzy}, \chi_{xxz} = \chi_{yyz}, \chi_{zxx} = \chi_{zyy}, \chi_{zzz}$). Here, the subscripts on χ are the Cartesian directions in the laboratory frame. [77, 80] By utilizing different polarization conditions, it is possible to probe directly three of the four nonvanishing susceptibility-tensor components independently. [25, 77, 80]

Each of the three light fields (with corresponding frequencies $\omega_{SFG}, \omega_{vis}, \omega_{IR}$) in SFG experiments can be either S or P polarized. S polarized light has a polarization vector parallel to the interface, and the P polarization is at an angle tilted to the surface and lies in a plane that is perpendicular to the interface. If the xy plane is taken to be the interface, it is usually defined that S polarized light has a single Cartesian polarization vector component along the y axis $b\hat{\boldsymbol{y}}$ while P the vector lies in the xz plane with components $c\hat{\boldsymbol{x}} + d\hat{\boldsymbol{z}}$. [77, 81] Different combinations of S and P polarized fields allow for direct measurement of the following tensor elements: [77, 80, 82]

$$\chi^{(2)}_{eff,SSP} = sin(\beta_{IR}) L_{yy}(\omega_{SFG}) L_{yy}(\omega_{vis}) L_{zz}(\omega_{IR}) \chi_{yyz} \tag{2.16}$$

$$\chi^{(2)}_{eff,SPS} = sin(\beta_{vis}) L_{yy}(\omega_{SFG}) L_{zz}(\omega_{vis}) L_{yy}(\omega_{IR}) \chi_{yzy} \tag{2.17}$$

$$\chi^{(2)}_{eff,PSS} = sin(\beta_{SFG}) L_{zz}(\omega_{SFG}) L_{yy}(\omega_{vis}) L_{yy}(\omega_{IR}) \chi_{zyy} \tag{2.18}$$

$$\chi^{(2)}_{eff,PPP} = -cos(\beta_{SFG}) cos(\beta_{vis}) sin(\beta_{IR}) L_{xx}(\omega_{SFG}) L_{xx}(\omega_{vis}) L_{zz}(\omega_{IR}) \chi_{xxz} \tag{2.19}$$

$$-cos(\beta_{SFG}) sin(\beta_{vis}) cos(\beta_{IR}) L_{xx}(\omega_{SFG}) L_{zz}(\omega_{vis}) L_{xx}(\omega_{IR}) \chi_{xzx}$$

$$+sin(\beta_{SFG})cos(\beta_{vis})cos(\beta_{IR})L_{zz}(\omega_{SFG})L_{xx}(\omega_{vis})L_{xx}(\omega_{IR})\chi_{zxx}$$

$$+sin(\beta_{SFG})sin(\beta_{vis})sin(\beta_{IR})L_{zz}(\omega_{SFG})L_{zz}(\omega_{vis})L_{zz}(\omega_{IR})\chi_{zzz}$$

Here, L represents the Fresnel factors for the given fields (linear Fresnel factors for the visible and IR fields and a nonlinear factor for the sum frequency field) [23], and $\beta(\omega_i)$ is the angle that the field at frequency ω_i makes with respect to the surface normal. We use $\chi^{(2)}_{eff}$ to denote the effective susceptibility - unlike $\chi^{(2)}_{ijk}$, $\chi^{(2)}_{eff}$ explicitly accounts for the Fresnel factors. The S and P indicies on $\chi^{(2)}_{eff,\alpha\beta\gamma}$ denote how the fields ω_{SFG}, ω_{vis}, and ω_{IR} respectively are polarized - *i.e.*, S or P. In the above expressions, because of the chosen experimental geometry, three of the polarization conditions (SSP, SPS, PSS) directly probe single susceptibility tensor components while the PPP condition has components of all unique *allowed* Cartesian tensor elements.

2.3 Wave Vector and Phase-Matching Considerations

In coherent nonlinear optical experiments, the signal is generated at a well defined angle in the laboratory frame that is determined by the wave vector of the incident radiation. However, only certain experimental geometries will generate a desired $\mathbf{P}^{(N)}(\mathbf{k_s})$ signal. The required geometries must satisfy phase-matching conditions that are a consequence of the input-wave-vector choice. To understand the phase-matching conditions that need to be met, consider a monochromatic plane wave, $exp\,(i\mathbf{k_j}\cdot\mathbf{r}-i\omega_j t)$, and its associated wave vector, $\mathbf{k_j}$. Its frequency, ω_j, and wave vector are related by the complex refractive index, $n(\omega_j)$=Re$\{n(\omega_j)\}$+i Im$\{n(\omega_j)\}$: [58, 62]

$$\mathbf{k_j} = \frac{n(\omega_j)\omega_j\mathbf{u_j}}{c} \tag{2.20}$$

Here, c is the speed of light in vacuum, and $\mathbf{u_j}$ is a unit vector which gives the direction of the wave vector. Each applied field then has an angle of incidence, θ_j, and a distinct time-dependent phase, ϕ_j, associated with it (see Figure 2.1):

$$\phi_j(t) = \frac{Re\{n(\omega_i)\}\omega_j}{c}\mathbf{u_j} \cdot \mathbf{r} - \omega_j t \tag{2.21}$$

In the context of second-order experiments, when the two incident wave vectors of the applied fields at an interface add, $\mathbf{k_1} + \mathbf{k_2}$, a SFG signal is generated. Alternatively, when $\mathbf{k_s} = \pm\mathbf{k_1} \mp \mathbf{k_2}$ a DFG signal is generated. Because the incident field's wave vectors are overlapped at the medium's interface, the field associated with $\mathbf{k_s}$ will be transmitted through the medium and also reflected from the surface of the medium (except for the case of total internal reflection). In the electric dipole approximation (in isotropic media), both the reflected and transmitted signals are interface specific. If bulk quadrupolar contributions are important, the transmitted signal may contain a significant contribution from the bulk that is not always separable from the interfacial signature. [45,46,83] Snell's Law, in conjunction with medium-specific properties and the incident field's wave vectors, must be considered when determining the wave vector of the reflected, $\mathbf{k_s^{(r)}}$, and transmitted, $\mathbf{k_s^{(T)}}$, signals.

It should be noted, although the two incident field's wave vectors initially may combine to give $\mathbf{k_1} + \mathbf{k_2}$ and/or $\mathbf{k_s} = \pm\mathbf{k_1} \mp \mathbf{k_2}$, it is not guaranteed a measurable signal will be reflected. This is due to phase-matching conditions, a consequence of energy and momentum conservation, that must satisfied. This consideration leads to SFG and DFG signals only being detectable at angles that satisfy the following equations (in a typical

SFG experimental geometry detailed in Figure 2.1): [62]

$$sin(\theta_{SFG}) = \frac{\omega_1 sin(\theta_1) + \omega_2 sin(\theta_2)}{\omega_1 + \omega_2} \tag{2.22}$$

$$sin(\theta_{DFG}) = \frac{\omega_1 sin(\theta_1) - \omega_2 sin(\theta_2)}{\omega_1 - \omega_2} \tag{2.23}$$

Note, although Equation 2.22 always has a solution, Equation 2.23 does not. Specifically, for the given conditions, this means SFG will *always* emit a signal while DFG will emit a signal only when Equation 2.24 is satisfied:

$$\left(\frac{\omega_1 sin(\theta_1) - \omega_2 sin(\theta_2)}{\omega_1 - \omega_2}\right)^2 \leq 1 \tag{2.24}$$

2.4 $\boldsymbol{\chi}(\omega_1, \omega_2)$ in the Dipole Approximation

The system's susceptibility, $\boldsymbol{\chi}$, contains all the optical information about the material system, and, is thus, the focus of theoretical investigations into SFG interfacial vibrational spectroscopy. In order to calculate $\boldsymbol{\chi}$, or equivalently the system-response function, $\mathbf{R}^{(2)}$, it is necessary to develop a microscopic description of it. Further, it is desirable to represent the response function in a form amenable to calculation, and one that can exploit the power of MD interfacial simulations. MD is capable of accurately describing both the structure and dynamics of even complex interfaces. [2–6, 10–13, 84–86] Specifically, it will be shown the SFG response function is proportional to the imaginary part of the one-time cross-correlation function of the system dipole and polarizability. [1–5, 7]

In order to pursue this goal, starting from density-matrix theory, and using perturbative techniques, a formal expression for the second-order susceptibility in the dipole approximation can be derived. [5, 25, 58, 87] Using this method, $\chi_{ijk}^{(2)SFG}(\omega)$ is defined by

a sum of six terms (shown below). [6, 58] Four of the terms contribute to the resonant SFG signal (contained in R_1 and R_2), and the remaining contribute to the nonresonant portion of the signal (NR_1 and NR_2). The two terms in R_2 contain the expressions $(\omega_{IR} + \omega_{ng} + i\gamma_{ng})$, and may initially appear to be nonresonant; γ is an arbitrary convergence parameter in time [88] that is frequently interpreted physically as a dipole-dephasing rate [6, 58] that would be responsible for a single mode's homogeneous line width in the frequency domain. Inclusion of these terms in the resonant susceptibility is, however, necessary to develop a general theory. Neglecting these contributions results in an expression valid only when $\hbar\omega \ll kT$, where k is Boltzmann's constant and T is the system temperature (this is equivalent to making the RWA in this case). Note, although we use ω_{IR} and ω_{vis}, this is easily generalizable to two arbitrary applied fields.

In the frequency domain, $\chi^{(2)SFG}_{pqr}(\omega)$ takes the form

$$\chi^{(2)SFG}_{pqr}(\omega_{SFG}, \omega_{vis}, \omega_{IR}) = \sum_{g,n,m} (\rho^{(0)}_g)(R_1 + R_2 + NR_1 + NR_2) \tag{2.25}$$

$$R_1 = \left(\frac{\mu^p_{gn}\mu^q_{nm}}{(\omega_{SFG} - \omega_{ng} + i\gamma_{ng})} - \frac{\mu^q_{gn}\mu^p_{nm}}{(\omega_{vis} + \omega_{ng} + i\gamma_{ng})} \right) \left(\frac{\mu^r_{mg}}{(\omega_{IR} - \omega_{mg} + i\gamma_{mg})} \right)$$

$$R_2 = \left(\frac{\mu^q_{nm}\mu^p_{mg}}{(\omega_{SFG} + \omega_{mg} + i\gamma_{mg})} - \frac{\mu^p_{nm}\mu^q_{mg}}{(\omega_{vis} - \omega_{mg} + i\gamma_{mg})} \right) \left(\frac{\mu^r_{gn}}{(\omega_{IR} + \omega_{ng} + i\gamma_{ng})} \right)$$

$$NR_1 = \frac{\mu^q_{gn}\mu^p_{mg}\mu^r_{nm}}{(\omega_{SFG} + \omega_{mg} + i\gamma_{mg})(\omega_{vis} + \omega_{ng} + i\gamma_{ng})}$$

$$NR_2 = \frac{\mu^p_{gn}\mu^q_{mg}\mu^r_{nm}}{(\omega_{SFG} - \omega_{ng} + i\gamma_{ng})(\omega_{vis} - \omega_{mg} + i\gamma_{mg})}$$

In the above expressions that define the six components of the second-order susceptibility, ω_{ng} is the frequency corresponding to the energy difference between energy levels n and

g. In Equation 2.25, $\rho_g^{(0)}$ is the initial-state thermal population, and the sum is over vibronic levels. $\mu_{\alpha,\beta}^{\eta}$ is a dipole matrix element between states α and β for dipole vector component η.

Approximating $1/\omega_{sfg} \approx 1/\omega_{vis}$, the resonant contributions can be simplified by rewriting them in terms of polarizabilities and dipoles. Given the definition of polarizability in Equation 2.26, the two resonant terms, R_1 and R_2, simplify to Equations 2.27 and 2.28 respectively:

$$\alpha_{pq}(\omega) = \sum_{g,n} \left[\frac{\mu_{gn}^{p}\mu_{ng}^{q}}{-\omega + \omega_{ng} - i\gamma_{ng}} + \frac{\mu_{gn}^{q}\mu_{ng}^{p}}{\omega + \omega_{ng} + i\gamma_{ng}} \right] \rho_g^{(0)} \tag{2.26}$$

$$R_1 = -\frac{\alpha_{gm}^{pq}\mu_{mg}^{r}}{(\omega_{IR} - \omega_{mg} + i\gamma_{mg})} \tag{2.27}$$

$$R_2 = -\frac{\mu_{gn}^{r}\alpha_{ng}^{pq}}{(\omega_{IR} + \omega_{ng} + i\gamma_{ng})} \tag{2.28}$$

Let χ_{pqr}^{Res} denote only the sum of the resonant terms R_1 and R_2. Replacing the denominators in both of the resonant terms with the integral identities $\int_0^\infty dt\ e^{-it(\omega-\omega_o-i\gamma)} = \frac{-i}{\omega-\omega_o-i\gamma}$ and $\int_0^\infty dt\ e^{it(\omega+\omega_o+i\gamma)} = \frac{i}{\omega+\omega_o+i\gamma}$, and then taking the implied limit that gamma goes to zero, gives Equation 2.29. Equation 2.30 follows as an exact rewrite of Equation 2.29, and expresses the susceptibility in terms of the cross correlation of the system dipole and polarizability:

$$\chi_{pqr}^{Res} = \left[\frac{i}{\hbar} \sum_{gm} \int_0^\infty e^{-i\omega_{mg}t} e^{i\omega_{IR}t} \alpha_{gm}^{pq}\mu_{mg}^{r} dt - \frac{i}{\hbar} \sum_{ng} \int_0^\infty e^{i\omega_{ng}t} e^{i\omega_{IR}t} \alpha_{ng}^{pq}\mu_{gn}^{r} dt \right] \rho_g^{(0)} \tag{2.29}$$

$$\chi_{pqr}^{Res} = \frac{i}{\hbar} \int_0^\infty dt\ e^{it\omega_{IR}} < \alpha_{pq}(t)\mu_r(0) > - \frac{i}{\hbar} \int_0^\infty dt\ e^{it\omega_{IR}} < \mu_r(0)\alpha_{pq}(t) > \tag{2.30}$$

In deriving Equation 2.29 from 2.30, $\alpha_{pq}(t)$ is identified as the Heisenberg representation of the polarizability operator α at time t, and a sum over states is performed to remove a resolution of the identity. [89, 90]

Expressing the correlation function in Equation 2.30 explicitly as the sum of its real and imaginary components reduces Equation 2.30 to Equation 2.31, below. Note, $< \mu_r(0)\alpha_{pq}(t) >= C_R(t) + iC_I(t) = (< \alpha_{pq}(t)\mu_r(0) >)^*$, and the subscripts R and I will be used throughout the manuscript to represent the real and imaginary parts (both of which are themselves real) of complex quantities. [89] In the frequency domain the TCF is real, and takes the form $C(w) = C_R(\omega) + C_I(\omega)$ – where C_R is even ($C_R(\omega)$=$C_R(-\omega)$) while $C_I(\omega)$ is odd ($-C_I(\omega)$=$C_I(-\omega)$): [89, 91, 92]

$$\chi^{Res}_{pqr}(\omega_{IR}) = \frac{2}{\hbar}\int_0^\infty dt e^{it\omega_{IR}} C_I(t) \tag{2.31}$$

Note, χ^{Res}_{pqr} is presented as an explicit function of the IR frequency because the other optical frequencies are absorbed implicitly into the polarizability. Equation 2.31 is a nearly exact rewrite (exact other than substituting $1/\omega_{sfg} \approx 1/\omega_{vis}$) of the perturbation expression, and is the central result of this section; it links the susceptibility to a TCF of the system's dipole and polarizability. The quantum-mechanical TCF is amenable to calculation using classical MD supplemented by a suitable spectroscopic model *via* quantum correcting the classical TCF; [3, 93, 94] while Equation 2.31 includes the imaginary part of the TCF, classical TCF methods can only approximate the real part, but as will be detailed below, the real and imaginary parts of the TCF are simply related in the frequency domain. [95, 96]

The literature contains examples of using an expression similar to Equation 2.31, but

written in the RWA. [5,12,14] It will now be demonstrated that only in the high-frequency limit, and because of the exact frequency relationship between the real and imaginary components of the correlation function, can R_2 be excluded from the resonant component of the susceptibility. In this approximation, the resonant susceptibility is given by only the first term in Equation 2.29 – *i.e.*, the resonant susceptibility is then given as the Fourier transform of the full TCF:

$$\chi^{Res}_{pqr} = \frac{i}{\hbar}\sum_{gm}\int_0^\infty e^{-i\omega_{mg}t}e^{i\omega_{IR}t}\alpha^{pq}_{gm}\mu^r_{mg}\ dt = \frac{i}{\hbar}\int_0^\infty dt\ e^{i\omega_{IR}} < \alpha_{pq}(t)\mu_r(0) > \qquad (2.32)$$

To proceed, the correlation function is expressed as its real and imaginary time-dependent components. Next, both the real and imaginary components of the correlation function are represented as their corresponding Fourier transforms, and the order of integration is switched:

$$\chi^{Res}_{pqr} = \frac{i}{\hbar}\int_0^\infty dt\ e^{i\omega_{IR}t}(C_R(t) - iC_I(t)) \qquad (2.33)$$

$$\chi^{Res}_{pqr} = \frac{i}{2\pi\hbar}\int_0^\infty dt\ e^{i\omega_{IR}t}\int_{-\infty}^\infty d\omega\ e^{i\omega t}C_R(w) + \frac{1}{2\pi\hbar}\int_0^\infty dt\ e^{i\omega_{IR}t}(-i)\int_{-\infty}^\infty d\omega\ e^{i\omega t}C_I(w) \qquad (2.34)$$

$$\chi^{Res}_{pqr} = \frac{i}{2\pi\hbar}\int_{-\infty}^\infty d\omega\ C_R(w)\int_0^\infty dt\ e^{it(\omega_{IR}+\omega)} - \frac{i}{2\pi\hbar}\int_{-\infty}^\infty d\omega\ C_I(w)\int_0^\infty dt\ e^{it(\omega_{IR}+\omega)} \qquad (2.35)$$

The integration over dt in Equation 2.35 can easily be performed and results in a delta function and principal-part contribution: [88]

$$\chi^{Res}_{pqr} = \frac{i}{2\hbar}C_R(\omega_{IR}) + \frac{i}{2\hbar}C_I(\omega_{IR}) + \frac{P}{2\pi\hbar}\int_{-\infty}^\infty d\omega\ \frac{C_I(\omega) + C_R(w)}{\omega_{IR} + \omega} \qquad (2.36)$$

Equation 2.36 contains the Fourier transforms of both the real and imaginary parts of the TCF in contrast to the exact result; Equation 2.31 (after performing the time integration) is proportional to only the sum of the Fourier transform of the imaginary part of the TCF plus a principal-part contribution. However, because there exists an exact detailed-balance relationship between the real components of the frequency-domain correlation function, $C_I(w) = tanh(\beta\hbar\omega/2)C_R(w)$, Equation 2.36 can be rewritten as

$$\chi^{Res}_{pqr} = \frac{i}{2\hbar}[1 + coth(\beta\hbar\omega_{IR})]C_I(\omega_{IR}) + \frac{P}{2\pi\hbar}\int_{-\infty}^{\infty} d\omega \; \frac{C_I(\omega) + coth(\beta\hbar\omega/2)C_I(w)}{\omega_{IR} + \omega} \quad (2.37)$$

In the high frequency limit, where $coth(\beta\hbar\omega/2) \rightarrow 1$, Equation 2.37 is the correct expression relating the resonant susceptibility to the imaginary component of the correlation function.

Equation 2.32 has been used in the literature to calculate the resonant susceptibility, and, in those cases, the full quantum TCF is approximated as the classical TCF. [6, 12] Equation 2.32 is accurate at sufficiently high frequency, but when adopting a classical approach, it is better to link the classical correlation function to the quantum TCF *via* quantum-correction approaches [2, 3, 97] – although quantum correction affects the magnitude of the signal more than the lineshape. Further, Equation 2.32 is not accurate at lower frequencies where many interesting interfacial phenomena occur. [98] However, to date, SFG experiments have focused on high-frequency intramolecular vibrations due to technical limitations – most tunable IR lasers are not yet capable of probing lower frequencies. Even though some nonlinear crystals (*e.g.* GaSe) can generate infrared beams with strong enough intensity in the lower wavenumbers, they are not widely applied, and current typical SFG experiments employ optical-parametric-amplifier (OPA) generated

tunable IR radiation that has insufficient power to create measurable SFG signals below about 1000 cm^{-1}. [18, 53, 99] There are, however, free-electron laser sources that produce sufficiently intense light for SFG experiments into the far IR. [98] Computationally, these regions of lower frequency can be analyzed, [2, 3] and have revealed novel low-frequency species present at the water/vapor interface. [2, 3, 8]

Chapter 3

Time Correlation Function Theory

MD is often used to calculate thermodynamic equilibrium properties. In addition, perturbations of equilibrium systems may also be examined in linear-response theory. Central to this idea is the fluctuation-dissipation theorem, which states that the relaxation of small perturbations of a system can be related to the fluctuations that occur spontaneously in equilibrium systems. This (Onsager's) hypothesis earned Lars Onsager the 1968 Nobel Prize in chemistry. [100]

3.1 Theoretical Development

Fluctuations in an observable about the equilibrium ensemble average $< A >$ (where the angle brackets indicate ensemble average) can be written as

$$\delta A(t) = A(t) - < A > \tag{3.1}$$

Now, we know that $< \delta A >= 0$, but if we correlate $\delta A(t)$ to a spontaneous fluctuation at time zero,

$$C(t) =< \delta A(0)\delta A(t) >=< A(0)A(t) > - < A >^2 \tag{3.2}$$

we can show that at short times

$$C(0) =< \delta A(0)\delta A(0) >=< \delta A^2 > \tag{3.3}$$

Whereas at long times, $\delta A(t)$ becomes uncorrelated to $\delta A(0)$:

$$C(t) \rightarrow < \delta A(0) >< \delta A(0) > \tag{3.4}$$

But we know that $< \delta A >= 0$, so at long times $C(t) \rightarrow 0$. This decay of correlation with increasing time is the regression of spontaneous fluctuations and can be related to the relaxation of a system from a perturbation. The Hamiltonian for this system is H, and the equilibrium average of the observable can be written as the trace of the observable:

$$< A > \;=\; \frac{\mathrm{Tr}e^{-\beta H}A}{\mathrm{Tr}e^{-\beta H}} \tag{3.5}$$

If we perturb the system at time $t = 0$ with $\delta H = -fA$, where f is an applied field that couples to A, we can follow the relaxation of $A(t)$ back to $< A >$:

$$\begin{aligned} A(0) &= \frac{\mathrm{Tr}e^{-\beta H+\delta H}A}{\mathrm{Tr}e^{-\beta H+\delta H}} \\ A(t) &= \frac{\mathrm{Tr}e^{-\beta H+\delta H}A(t)}{\mathrm{Tr}e^{-\beta H+\delta H}} \end{aligned} \tag{3.6}$$

If we expand $A(t)$ about δH, and note that classically H and δH commute we obtain

$$\begin{aligned} A(t) &= \frac{\mathrm{Tr}[e^{-\beta H}(1-\beta\delta H+...)\times A(t)]}{Tr[e^{-\beta H}(1-\beta\delta H+...)]} \\ &= \frac{Tr[e^{-\beta H}(A(t)-\beta\delta HA(t)+A(t)\mathrm{Tr}e^{-\beta H}(\beta\delta H)/\mathrm{Tr}e^{-\beta H})]}{\mathrm{Tr}e^{-\beta H}+O((\beta\delta H)^2)} \\ &= < A > -\beta[< \delta HA(t) > - < A >< \delta H >] + O((\beta\delta H)^2) \end{aligned} \tag{3.7}$$

Using equation 3.1 and inserting the expression for δH, we have [100]

$$\delta A(t) = \beta f < \delta A(0)\delta A(t) > +O(f^2) \tag{3.8}$$

3.2 TCF Method for SFG Spectroscopy

The following is a derivation of a time-domain approach [1–3,5] to calculating the resonant susceptibility. At the core of this approach is calculating the cross TCF of the system dipole and polarizability, $< \alpha_{pq}(t)\mu_r(0) >$. This, being the product of a first and second rank tensor, vanishes in isotropic media. [101]

The resonant part of the susceptibility is given by the imaginary part of this quantum-mechanical TCF *via* Equation 2.31. The goal, in this context, is to rewrite Equation 2.31 in a form that is amenable to calculation using classical TCF theory in order to take advantage of the power of the molecularly detailed description offered by many-body classical MD. To proceed, the imaginary part of the one-time TCF is related in frequency space exactly to the real part: $C_I(\omega) = tanh(\beta\hbar\omega/2)C_R(\omega)$; where the subscripts denote the Fourier transform of the real and imaginary parts of the complex function $C(t)$ which is a real function of frequency, *i.e.* $C(\omega) = (\frac{1}{2\pi})\int_{-\infty}^{\infty} dt e^{-i\omega t}(C_R(t) + iC_I(t)) = C_R(\omega) + C_I(\omega)$. Substituting into Equation 2.31 gives

$$\chi^{Res}(\omega) = \frac{2}{\hbar}\int_0^{\infty} dt e^{i\omega t} C_I(t) \tag{3.9}$$

$$C_I(t) = \int_{-\infty}^{\infty} d\omega' e^{i\omega' t} tanh(\beta\hbar\omega'/2) C_R(\omega')$$

Note, $C_I(t)$ is written in a form that can be calculated using the real part of the correlation function – which is approximately obtainable, after quantum correction, using classical MD and TCF approaches. Due to causality, the Fourier-Laplace transform gives a real and imaginary part in Equation 3.9 as the cosine and sine transform of $C_I(t)$ respectively. Equation 3.9 can be simplified by changing the order of integration – performing the

frequency-domain integral first. Defining the real and imaginary parts of $\chi^{Res}(\omega) = \chi_R^{Res}(\omega) + i\chi_I^{Res}(\omega)$:

$$\chi_I(\omega) = \frac{1}{\hbar} tanh(\beta\hbar\omega/2) C_R(\omega) = \frac{2}{\hbar}\int_0^\infty sin(\omega t) C_I(t) dt \tag{3.10}$$

$$\chi_R(\omega) = \frac{1}{\pi\hbar} P\int_{-\infty}^{\infty} \frac{tanh(\beta\hbar\omega/2) C_R(\omega')}{\omega+\omega'} d\omega' = \frac{2}{\hbar}\int_0^\infty cos(\omega t) C_I(t) dt \tag{3.11}$$

To obtain Equations 3.10-3.11, the identity $\int_0^\infty e^{i\omega t} dt = \frac{iP}{\omega} + \pi\delta(\omega)$ was used. P designates the principal part. [88]

The current focus of SFG experiments is on intramolecular vibrations, and to calculate observables in this spectral region, classical mechanics is clearly invalid. Building on our previous work, the classical correlation function result, which is amenable to calculation using MD and TCF methods, is quantum corrected using a "harmonic correction" factor: $C_R(\omega) = C_{Cl}(\omega)(\frac{\beta\hbar\omega}{2} coth(\beta\hbar\omega/2))$. [97, 102] This correction factor is exact in relating the real part of the classical harmonic coordinate correlation function to its quantum mechanical counterpart. It is worth noting it is not uncommon in modeling vibrational spectroscopy *via* TCFs to see the real part of the quantum TCF replaced by the classical TCF that has the same even time symmetry, and becomes equivalent classically (at low frequencies where $\hbar\omega \ll kT$). This approach is reasonable in describing vibrational lineshapes but does not give accurate intensities. It is generally better to use the harmonic correction factor. Similar caveats apply to replacing the full quantum TCF with its classical counterpart, but, in that case, one neglects the imaginary part of the TCF entirely (that may not matter very much when considering high-frequency phenomena for which $C_I(\omega) = C_R(\omega)$ because the hyperbolic tangent function is approaching unity).

Using the classical harmonic coordinate quantum correction factor does not account for the fact the dipole and polarizability contain higher orders of the coordinates – exact corrections for harmonic systems of this type are still possible, but unneeded (the linear dipole and Placzek approximation are adequate). [97] Using this result, the TCF approximation to the resonant part of the SFG spectrum, χ^{Res}, takes the form

$$\chi_I(\omega) = \beta\omega\pi C_{Cl}(\omega) \tag{3.12}$$

$$\chi_R(\omega) = \beta P \int_{-\infty}^{\infty} \frac{C_{Cl}(\omega')\ \omega'}{\omega + \omega'} d\omega' \tag{3.13}$$

$$C_{Cl}(t) =< \mu_i(0)\alpha_{jk}(t) > \tag{3.14}$$

In Equation 3.14, the angle brackets represent a classical TCF that can be computed using MD, and a suitable spectroscopic model. [5, 103] Finally, Equations 3.12-3.13 give the TCF signal in a form amenable to classical simulation. Note, while it easier to evaluate $\chi_I(\omega)$ using Equation 3.12, $\chi_R(\omega)$ is more easily computed by doing the cosine integral as in Equation 3.11. [3] Considering three possible independent polarization conditions, SSP, PPP, and SPS, for the TCF in Equation 3.14, the last index in the polarization designation corresponds to the first index in the TCF. For example, the SSP and PPP polarization conditions probe dipolar motions normal to the interface, and the SPS case is sensitive to dipolar changes parallel to the interface. Note, the PPP condition is sensitive to motions both parallel and perpendicular to the interface. [77] Further, the (SSP and PPP)/(SPS) probe diagonal/off-diagonal polarizability matrix elements respectively.

Chapter 4

Instantaneous Normal Mode Theory

INM theory has been successful in describing a number of liquid-state properties. [104–114] Further, INM theory is an intuitively appealing and effective approach to modeling interfacial spectroscopy. [1–3] The INM approach to spectroscopy can be interpreted as an approximation to the true Born-Oppenheimer vibrational density of states (DOS). [93] Spectroscopic quantities may be evaluated by making a harmonic oscillator approximation to the relevant frequency-domain golden-rule expression, leading to an approximation to the spectrum in the form of a weighted DOS (wDOS). For SFG spectroscopy this becomes a dipole and polarizability derivative weighted INM DOS, where the derivative of the dipole or polarizability is with respect to the INMs. The INM wDOS can be constructed from thermodynamic information, not requiring explicit dynamical input, although it contains short time dynamical information.

In several dense liquids, where rotations are significantly hindered, INM intermolecular spectra have been shown to be almost equivalent to TCF derived spectra, [115–121] and this has led to an interpretation of the intermolecular dynamics in the slow modulation limit of Kubo's motional narrowing theory. [55] Intramolecular line shapes can

be interpreted as being in the motionally-narrowed, fast-modulation limit, where the underlying INM "spectral density" is narrowed into a slimmer line shape. The Kubo theory of motional narrowing focuses on the line shape associated with a time-dependent harmonic oscillator, and it becomes simple in the limits of slow and fast modulation. In the slow-modulation limit the line shape reflects all the frequency fluctuations that the oscillator exhibits; in the fast-modulation (motionally-narrowed) regime the line shape is narrowed. In interpreting an INM wDOS in this context one assumes that INMs are well defined for some time [122, 123] and that they fluctuate in frequency. This kind of interpretation is suggested by the time dependence of the INM frequencies.

It will be shown that consistent with the Kubo picture, we have found that the intramolecular INM bands are broader but have the nearly the same central frequency as their corresponding TCF line shape, and the integrated intensities of the TCF and INM bands are approximately equal. [2–4] These two observations suggest the identification of the INM wDOS as an underlying spectral density, *i.e.* the intramolecular line shape with motional narrowing effects removed.

A major strength of the INM method is that it is a frequency-domain method, allowing for the modes at any given frequency to be analyzed in molecular detail. INM theory provides a tractable method for examining the underlying molecular motions responsible for generating the associated INM and presumably TCF spectroscopic signature. This is possible because, as noted above, INM intermolecular spectra are often in near agreement with corresponding TCF results; when concerned with intramolecular line shapes it is argued, that the INM spectrum still represents the underlying "spectral density" that is

motionally narrowed to give the observed line shape.

4.1 Theoretical Development

Interfaces are modeled via typical MD simulations in order to generate configurational ensembles that are representative of the potential energy landscape. The total potential energy of each configuration can be expanded as follows:

$$V = V(\boldsymbol{r}_0) + \sum_{i=1}^{N} \left(\frac{\partial V}{\partial r_i}\right)_{\boldsymbol{r}_0} r_i + \sum_{i,j=1}^{N} \left(\frac{\partial^2 V}{\partial r_i r_j}\right)_{\boldsymbol{r}_0} r_i r_j \tag{4.1}$$

The normal coordinates are obtained by diagonalizing the matrix of second derivatives of the potential energy, the Hessian matrix [104, 110, 119, 122, 124–127]:

$$D_{i,j} = \frac{\partial^2 V}{\partial q_i \partial q_j} \tag{4.2}$$

where $q_i = m_i^{1/2} \boldsymbol{r}_i$ is the mass-weighted coordinate for atom i with mass m_i, and position vector $\boldsymbol{r}_i$. Diagonalization of the force constant matrix yields a set of $3N$ eigenvalues which are the squares of the INM frequencies, ω^2. Imaginary INMs are those in which the eigenvalue is negative, therefore the frequency of the mode is imaginary. The corresponding eigenvectors map the system coordinates onto the INM coordinates Q, which have the following form:

$$Q_k = \sum_i u_{ik} q_i, \tag{4.3}$$

where u_{ik} is the i^{th} element of the eigenvector k. The INM approximation to the vibrational density of states (DOS) is a histogram of frequencies obtained over an ensemble average of configurations:

$$\rho(\omega) = \langle \sum_{k=1}^{3N} \delta(\omega - \omega_k) \rangle. \tag{4.4}$$

4.2 INM Method for SFG Spectroscopy

We constructed an INM approximation to SFG spectra. To do so, it is sufficient to evaluate Equations 3.12-3.14 for a harmonic system. To do so, it is convenient to invoke both the Placzek and linear-dipole approximation to evaluate the resulting matrix elements – although higher-order contributions can be included, and simple analytic expressions result for these contributions. An equivalent approach is to evaluate $C_{Cl}(t)$ for classical harmonic oscillators, and quantum correct the resulting expression using the harmonic-correction factor, $C_R(\omega) = C_{Cl}(\omega)(\frac{\beta\hbar\omega}{2} coth(\beta\hbar\omega/2))$, to relate $C_{Cl}(t)$ and $C_R(t)$:

$$C_{Cl}(\omega) =< (\partial\mu_i/\partial Q_l)\,(\partial\alpha_{jk}/\partial Q_l)\,\delta(\omega-\omega_l)\frac{kT}{\omega^2} > \tag{4.5}$$

In Equation 4.5, ω_l is the frequency of mode Q_l, and the angle brackets represent averaging over classical configurations of the system. $C_{Cl}(\omega)$ is then back transformed into the time domain, and used in Equations 3.12-3.13 in place of the classical TCF to obtain an INM approximation to the spectroscopy. It will be demonstrated the TCF approach, which does not invoke the Placzek and linear-dipole approximations (except implicitly in quantum correcting the results), gives results in close agreement with the INM results and Equation 4.5 is therefore sufficient.

Chapter 5

The Polarizability Model

In this work reference is made to the point atomic polarizability (PAPA) model [128,129]. In order to correctly model the system dipole, including both the permanent and induced-dipole contributions, polarization must be explicitly included in the calculations. Historically, polarizability had been treated as an additive quantity [130] whereby various atoms or functional groups were assigned empirical polarizabilities and their corresponding sum was the molecule's polarizability. However, this hypothesis is repeatedly criticized because this approach neglects the electric field induced by the induced dipoles themselves. Silberstein [131] overcame this objection by introducing a polarizability model which explicitly included the dipole-dipole interaction. This method was further developed by Applequist [128,129], avoiding perturbative approximations, and is the approach adopted in this work.

Consider a system of N atoms. In our point charge and PAPA model, [128, 129] each atom i has a point charge, q_i and a point polarizability, α_i. Each atom is polarized by an electric field, E_i^0. This gives rise to an induced-dipole moment, μ_i, which itself contributes to the total electric field E_i:

$$\mu_i = \alpha_i E_i \tag{5.1}$$

$$E_i = E_i^0 + \sum_{j \neq i} T_{ij}\mu_j \tag{5.2}$$

$$E_i^0 = \sum_j -\nabla_{r_i} \frac{q_j}{r_{ij}} \tag{5.3}$$

$$= \sum_j \frac{q_j r_{ij}}{r_{ij}^3} \tag{5.4}$$

where T_{ij} is the induced-dipole field tensor which has the form

$$T_{ij} = \nabla_{r_i} \nabla_{r_j} \frac{1}{r_{ij}} \tag{5.5}$$

$$T_{ij} = -\frac{3}{r_{ij}^5} \begin{bmatrix} x^2 & xy & xz \\ xy & y^2 & yz \\ xz & yz & z^2 \end{bmatrix} - \frac{1}{r_{ij}^3}\mathbf{I} \tag{5.6}$$

where r_{ij} is the distance between atoms i and j, and x, y, z are the vector components of r_{ij}. $\mathbf{I}$ is the identity matrix. Expanding equation 5.1 we get

$$\mu_i = \alpha_i \left[E_i^0 + \sum_{j \neq i}^{N} T_{ij}\mu_j \right] \tag{5.7}$$

which can be rewritten as

$$\alpha_i^{-1}\mu_i + \sum_{j=1, j \neq i}^{N} T_{ij}\mu_j = E_i \tag{5.8}$$

Equation 5.8 could be written in matrix form as

$$\begin{bmatrix} \alpha_1^{-1} & T_{12} & \cdots & T_{1N} \\ T_{21} & \alpha_2^{-1} & \cdots & T_{2N} \\ \vdots & \vdots & \vdots & \vdots \\ T_{N1} & \cdots & \cdots & \alpha_N^{-1} \end{bmatrix} \begin{bmatrix} \mu_1 \\ \mu_2 \\ \vdots \\ \mu_N \end{bmatrix} = \begin{bmatrix} E_1 \\ E_2 \\ \vdots \\ E_N \end{bmatrix} \tag{5.9}$$

or more briefly

$$\mathbf{A}\mu = \mathbf{E} \tag{5.10}$$

Here $\mathbf{A}$ is an $3N \times 3N$ real, symmetric matrix and μ and E are $3N \times 1$ column vectors. If we calculate the inverse of matrix $\mathbf{A}$, and write the inverse matrix $\mathbf{B}$ using 3×3 elements B_{ij}, then

$$\mathbf{B} = \begin{bmatrix} B_{11} & B_{12} & \cdots & B_{1N} \\ B_{21} & B_{22} & \cdots & B_{2N} \\ \vdots & \vdots & \vdots & \vdots \\ B_{N1} & \cdots & \cdots & B_{NN} \end{bmatrix} \tag{5.11}$$

Multiply Equation 5.10 by $\mathbf{B}$

$$\mu = \mathbf{BE} \tag{5.12}$$

This is a set of N linear equations

$$\mathbf{u}_i = \sum_{j=1}^{N} B_{ij} E_{ij}. \tag{5.13}$$

For our simulations and analysis, we may solve for the system's induced dipole M_{ind}, which is a sum of the individual induced dipoles, using either matrix inversion, or in an iterative, self-consistent fashion

$$M_{ind} = \sum_{i=1}^{N} \mu_i = \left[\sum_{i=1}^{N} \sum_{j=1}^{N} B_{ij} \right] E_i \tag{5.14}$$

From equation 5.14, we see that the induced dipole of the system, is merely a function of the inter-nuclear distances. However, when the interatomic distance r_{ij} approaches $(4\alpha_i\alpha_j)^{1/6}$, unphysically large values for the induced-dipole moments result. In order to correct this problem, a damping term is introduced.

In order to calculate the polarizability tensor of the system, we make the assumption of a constant electric field, E_i, and utilize Equations 5.1 and 5.13, to determine that

$$\alpha_{\mathbf{i}} = \sum_{j=1}^{N} B_{ij} \tag{5.15}$$

where previously, α_i was the scalar, point isotropic polarizability, which was dynamically coupled through chains of dipolar interactions, via the relay tensor B_{ij}. $\alpha_{\mathbf{i}}$ is the 3×3 polarizability tensor on atom i. No coupling exists between the local polarizability tensors; they are, generally speaking, more complex (anisotropic and possibly unsymmetric) and already contain the coupling between α_i's. From these tensors, we may now calculate the system polarizability tensor $\mathbf{A}$:

$$\mathbf{A} = \sum_{i=1}^{N} \sum_{j=1}^{N} B_{ij} \tag{5.16}$$

We now have the polarizability as a function of inter-nuclear distances. As with the system dipole, the polarizability tensor may be calculated using either matrix inversion or an iterative method.

The iterative method is derived from breaking up the polarizability tensor, in terms of the original isotropic point polarizabilities, α_i, and the dipole relay tensor T_{ij}. For a constant electric field, $\mu_i = \alpha_i E^0$. Substitution into equation 5.7 yields

$$\alpha_{\mathbf{i}} = \alpha_i^0 \mathbf{I} - \sum_{j \neq i} T_{ij} \alpha_{\mathbf{j}} \tag{5.17}$$

where we have used α_i^0 to denote the point isotropic polarizability.

Chapter 6

SFG Spectroscopy of the Water/Vapor Interface

In this chapter, classical MD methods are used to model the dynamics of the water/vapor interface. Two complementary theoretical approaches – quantum-corrected TCF and INM methods – use the configurations generated by MD as input to describe the SFG spectrum of the interface, and to ascertain the molecular origin of the SFG signal; both INM and TCF methods rely on a suitable spectroscopic (dipole and polarizability) model. This dual approach was demonstrated to be highly useful in understanding condensed phase spectroscopy of water, other liquids, and interfaces – classical mechanics, especially in the context of quantum-corrected TCFs, has proven to be surprisingly effective in modeling intramolecular vibrational spectroscopy. [1,2] In particular, TCF methods have provided a quantitative description of the O-H stretching lineshape in ambient liquid water, and INM methods have served to identify the molecular motions that result in the observed signal; these complementary techniques are equally effective for modeling water interfacial spectroscopy. [1–6, 94, 116–119, 132, 133]

An INM approximation to SFG spectroscopy is quantum mechanical by construction, but offers a limited dynamical description. As a result, in bulk water (and other liquid

state intramolecular lineshapes), INM intramolecular resonances are broader than their TCF counterparts, but have the same central frequency and integrated intensity. This suggests the intramolecular INM spectrum represents an underlying spectral density that is dynamically motionally narrowed in the actual lineshape. [55] This is also found to be the case here for SFG spectra in all polarization conditions. This result contrasts with a previous report by us, [1] and evidence from the literature. [5,6] Previous TCF and INM calculations of the (SSP polarization) SFG O-H stretching spectrum of the water/vapor interface were very noisy, and suggested the spectra had equal breadth – thus, suggesting motional narrowing effects were not apparent in the spectra. The success of an approximate, non-dynamical, frequency-domain technique, [6] and the similarity of the spectra to those obtained using TCF methods, [1, 5] appeared to be further evidence of spectra that could be described in the inhomogeneously-broadened limit. [122] That method, [6] however, contains an empirically adjustable line width that effectively accounts for some motional narrowing making it difficult to draw conclusions. Because of methodological advances, it is now possible to calculate well-averaged TCF and INM spectra, and they unambiguously demonstrate SFG O-H stretching lineshapes (at least at the water/vapor interface) are significantly motionally narrowed to a degree reminiscent of the bulk. [93, 134]

This suggests dynamical motional narrowing effects are important at interfaces, and the dynamics are best described as intermediate between the fast and slow modulation limits of motional narrowing. In the slow-modulation inhomogeneously-broadened limit, all frequency fluctuations of the oscillator are represented in the lineshape. [55, 122, 134]

A recent study in the Shen group also suggested motional averaging effects may well be significant in the SPS geometry, and, in that case, the free O-H stretching peak is greatly diminished. Although that study did not address motional narrowing, the presence of motional averaging suggests motional narrowing is important because it is due to fast reorientational motions within the vibrational relaxation time for the mode that would also be expected to result in motional narrowing.

In order to obtain better TCF results, long-time (cross) correlations between the system dipole and polarizability need to be followed. Because molecular simulations of interfaces in Cartesian space necessarily produce two interfaces, simulation times were limited to the molecular diffusion time between interfaces so molecules could not contribute to the signal at both interfaces during one MD run. [1] This leads to TCFs without long-time decays that are difficult to Fourier transform accurately. In this work, a weak restraining potential is added that confines the molecules over time to the half of the simulation box they start in (in the dimension normal to the interface) without significantly perturbing the (relevant short time) dynamics and average structure of the liquid that contributes to the interfacial spectroscopy; even though the molecular diffusion constant (normal to the interface) is changed, the molecule is only contributing to the spectrum while resident at the interface, and is free of any significant external potential.

This modification permits the calculation of TCFs out to arbitrarily long times – resulting in sharp spectra that include intermolecular spectral lineshapes. Surprisingly, a well-defined intermolecular mode was found to be prominent in the spectrum. [2] It is centered at 875. cm^{-1}, and is comparable in (integrated) intensity to the rest of the inter-

molecular lineshape – the lineshape also has an intensity that is approximately one-sixth of the magnitude of the intense free O-H stretching peak for spectra taken in polarization geometries that are sensitive to dipole derivatives normal to the interface (SSP and PPP). Using INM methods, the resonance is shown to be due to a wagging mode localized on individual water molecules. Water molecules contributing to this resonance are at a slight angle to the interface with their oxygen atoms anchored in the interface, and the hydrogen atoms wagging nearly normal to the interface. The presence of another population, aside from the free O-H stretch, of interfacial molecules was recently proposed *via* indirect evidence, [8,43,44] and that hypothesis is strongly supported by this work. Here, we have directly observed a spectroscopically distinct species, and clearly identified the vibrational mode responsible for the lineshape. Thus, experimental setups that permit taking spectra at relatively low wavelengths could probe this mode as a compliment to the information contained in the free and donor O-H stretching modes. At lower frequencies, well-defined hindered translational modes are found both parallel and perpendicular to the interface. The perpendicular modes are prominent in the polarization conditions sensitive to dipolar changes normal to the interface (SPP and PPP) while the parallel modes are more pronounced in the SPS geometry which is sensitive to motions along the interface.

Here, it is shown by carefully examining the real and imaginary parts of the SFG signal, individual mode contributions to an observed lineshape can be identified. Using this approach, the free O-H and the newly discovered modes were identified as individual spectroscopic species (one type of oscillator at the interface), and the "donor" O-H region

consists of three distinct species. This last conclusion agrees with results from a careful deconvolution of O-H stretching signal in an earlier experimental work that also found three species – each with approximately the same central frequency. [20]

Thus, as a prelude to more complex interfaces, this joint TCF/INM approach is applied to the water/vapor interface producing good agreement with the shape and relative amplitudes of SFG measurements for all independent polarization conditions. [15] The MD, dipole, many body polarization methods, and associated parameters are also summarized in Section 6.1. The theoretical results, and their comparison to experiment, are discussed in Section 6.2.

6.1 Simulation Models and Methods

MD simulations were performed using a code developed at the Center for Molecular Modeling at the University of Pennsylvania, and uses reversible integration and extended system techniques. [135] Microcanonical MD simulations were performed on ambient H_2O with a density of 1.0 g /cm^3, and an average temperature of 298K. To create an interface, a cubic simulation box of equilibrated liquid water was extended (doubled) along the z axis, and the system was allowed to equilibrate creating two water/vapor interfaces. The interfaces were sufficiently far apart so as they did not interact strongly, and Ewald summation was included in three dimensions. [11] The density profile of the system was monitored to verify equilibration. [11] In all cases, the results were tested, and found to be system size independent. Most results were generated from 216 molecule simulations, and smaller system sizes down to 64 molecules were tried, and did not alter

the results. [2]

MD simulations were conducted using a flexible simple point charge (SPC) model that included a harmonic bending potential, linear cross terms and Morse O-H stretching potentials, $V(r) = D_e(1 - e^{-\rho r})^2$. [93] The Morse O-H stretching potential used here was slightly softer than previous work; our ρ value is $2.50185\mathring{A}^{-1}$ instead of $2.566\mathring{A}^{-1}$. [1,93] For a Morse potential, the force constant, k, can be approximated as $k = 2D_e\rho^2$. Assuming a harmonic oscillator with frequency $\omega = \sqrt{\frac{k}{m}}$, this implies the ratio ρ_1:ρ_2 is proportional to the ratio ω_1:ω_2. Therefore, a 2.5% change in the exponential Morse parameter implies a 2.5% shift in the spectral frequencies, and this behavior is demonstrated in Figure 6.1. This analysis assumes the relevant coordinates are simple one dimensional O-H stretching modes. If several distinctly different types of modes were present, a change in the shape of the broad O-H stretching signal would be expected. This is additional evidence that interfacial normal modes are well approximated as simple O-H stretches. [1,2,6]

Figure 6.1 highlights the spectral changes resulting from using a softer Morse potential. The slightly softer potential does not alter the intermolecular region of the spectra as would be expected. The intermolecular portion of the spectrum has polarizability and dipole derivatives (changes) that are due primarily to reorientation. These changes then depend on the polarizability tensor and the dipoles themselves, and not their derivatives. On the other hand, the intramolecular region of the spectra is simply shifted to the red – this point will be returned to when discussing the modal composition of the broad O-H stretching lineshape. This change resulted in the free O-H stretching frequency in better

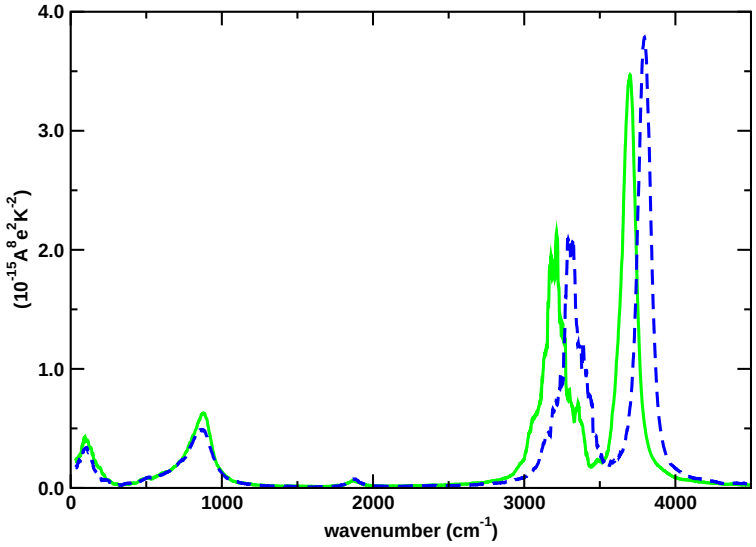

Figure 6.1: Different Potentials Change Spectra. SFG SSP TCF spectra for the water/vapor interface highlighting the spectral changes in the use of two different Morse potentials – the original Morse potential (dashed blue line), and a softer Morse potential (solid green line). The softer potential results in a shift of approximately 100. cm^{-1} in the O-H stretching spectrum.

agreement with experimental values even though the Morse potential change is almost imperceptible to the naked eye. This implies the center of the lineshape is very sensitive to the local frequency along the Morse potential as the O-H stretching motion, perturbed by hydrogen bonding in the liquid, explores the highly anharmonic potential surface.

In performing the MD, partial point charges were placed on the atoms that were chosen to reproduce the condensed phase dipole moment. At the water/vapor interface, the true water dipole falls from its condensed phase value, about 2.9 Debeye, to that

in the gas phase, 1.8 Debeye, over a distance of only a few molecular layers. [86] It would seem polarizable dynamics would be essential to model the dynamics of aqueous interfaces, but the use of non-polarizable MD seems to adequately represent the structure of the water/vapor interface. A previous work using a polarizable model in this context is consistent with this observation. [5]

Evaluating the TCF in Equations 3.12-3.14 presents a problem for interfacial systems. The interface was constructed using the standard MD geometry with vacuum/vapor above and below the water. [6,10] Unfortunately, this produces two interfaces with average net dipoles in opposite directions. Calculating the SFG spectrum of the entire system would lead to partial cancellation of the SFG signal, and meaningless results. Another problem arises in that molecules at one interface can diffuse to the other interface over time. In this case, simulation times are limited to the molecular diffusion time between interfaces so that molecules cannot contribute to signal at both interfaces during one MD run. This leads to TCFs without long-time decays that are difficult to Fourier transform accurately. [1, 5]

In order to obtain better TCF results, long-time (cross) correlations between the system dipole and polarizability need to be followed. A weak (laterally isotropic) restraining potential was added effectively confining the molecules over time to the half of the simulation box they start in (in the dimension normal to the interface) without significantly perturbing the relevant short time dynamics; even though the molecular diffusion constant (normal to the interface) is changed, the molecule is only contributing to the spectrum while resident at the interface, and is free of any significant external potential.

This modification permits the calculation of TCFs out to arbitrarily long times resulting in sharp spectra that include intermolecular spectral lineshapes. The restraining potential is of the form $V = \epsilon * (\sigma/r)^9$ with $\epsilon = 2.3$K, $\sigma = 2.474$Å, and $r = 0$ is at the center of the box. The restraining potential becomes negligible near the interface, and is only significant within ≈ 2.0 Å of the box center. The interfacial density profile was unchanged – demonstrating the restraining potential used did not perturb the average structure of the liquid that contributes to the interfacial spectroscopy.

The MD was performed without explicit polarization forces; when the SFG TCF or INM spectrum are calculated, polarizability is included in the calculations – over 3 million 3 fs time steps were included in calculating the MD and TCFs. The model employed includes full many-body polarization effects included explicitly *via* a PAPA polarizability model [128, 129, 136] with point polarizabilities on the atoms ($\alpha_O = 1.1482\mathring{A}^3$, $\alpha_H = 0.3304\mathring{A}^3$). [137] The permanent dipoles were calculated based on *ab initio* data. [1,5] The SFG signal is sensitive to both dipole and polarizability derivatives. PAPA polarizability models naturally incorporate parameters that determine the polarizability derivatives. To implement this, it is sufficient to make the point polarizabilities on the atomic centers (O-H) bond length dependent. [128, 129, 136] The point polarizabilities then change as: $\alpha(r) = \alpha_0(r) + \alpha'\Delta r$. Δr is displacement from the equilibrium bond length. The α' parameters for hydrogen and oxygen ($\alpha'_O = 2.7\mathring{A}^2$,$\alpha'_H = -1.06\mathring{A}^2$) are somewhat different than in our previous model, but still give reasonable values for the gas phase Raman and IR transition moments. [1] Figure 6.2c highlights the differences between the previous and current model for the SFG SSP TCF spectra.

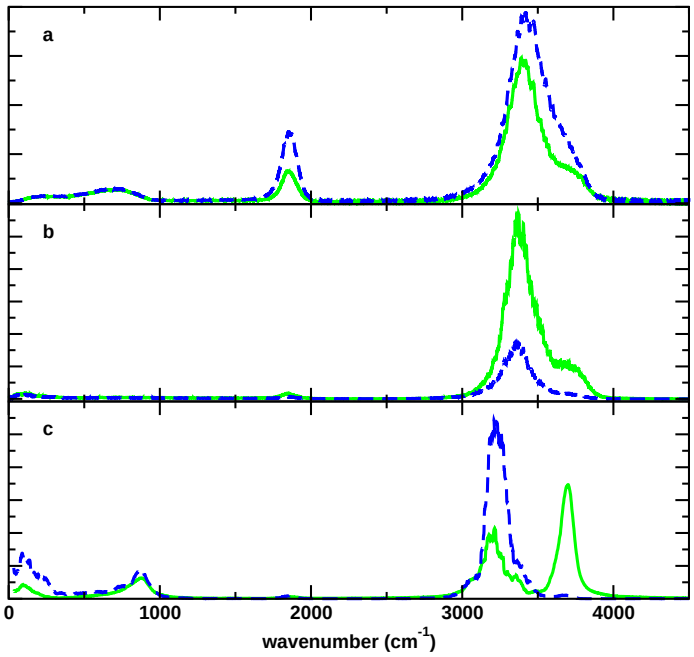

Figure 6.2: Different Polarizability Models Change Spectra. The (a) IR TCF spectra for liquid water, the (b) isotropic Raman TCF spectra for liquid water, and the (c) SFG SSP TCF spectra for the water/vapor interface highlighting the spectral changes in the use of two polarizability models – previous model (dashed blue line) and current model (solid green line).

It is interesting to note the new model captures the free O-H mode more accurately without significantly perturbing the intermolecular region of the spectra – intramolecular spectra are sensitive to dipole and polarizability derivatives that do not significantly change the magnitude of the dynamically more important dipole and polarizability. (Note, the small differences in the intermolecular spectrum are likely due to the relatively poor averaging that was done in calculating the spectrum using the previous model. In this case only one-fifteenth of the number of configurations were included in

the calculation, and the SFG TCFs were slow to converge. [1, 14]) Thus, even relatively small changes to these derivatives can greatly effect the spectroscopic observable without changing the essential physics of the problem – *e.g.*, the identity of the relevant modes and motions.

Figure 6.2 also presents the (a) infrared and (b) isotropic Raman TCF spectra (relevant to the SSP polarization condition because it probes diagonal elements of the polarizability matrix) for liquid water using both models. Again, only the intramolecular region of the spectra changed. For the O-H stretching region, increased asymmetry in the lineshape is apparent for the new model with a shoulder on the blue side. This is consistent with previous work that identified this shoulder to be due to instances in which a hydrogen does not form a hydrogen bond in the bulk [138, 139]; this would be analogous to the free O-H stretch found in interfacial spectra. The new polarizability model does a better job at highlighting this non-hydrogen bonded frequency distribution for liquid water, and, consequently, allows for more accurate interfacial spectra. The figure also clearly demonstrates the power of calculating spectroscopic observables to analyze condensed phase and interfacial structure. Interestingly, the shoulder on the blue side of the bulk Raman and IR spectrum is at the same central frequency as the free O-H mode at the interface – strongly suggesting the presence of free, non-hydrogen bonded, O-H modes in bulk water.

6.2 Results

Figure 6.3 displays the theoretical SFG SSP spectra for the entire water vibrational spectrum derived from both TCF and INM methods. Both the TCF and INM results are in absolute units, and no parameters were adjusted in displaying the data. The INM and TCF spectra were found to integrate to the same value over the entire 0. - 5000. cm^{-1} range, and separately over the O-H stretching region (2000. - 5000. cm^{-1}) for all polarization conditions (the others are not shown). This behavior is strong evidence for the interpretation of the INM lineshape as an underlying spectral density that is motionally narrowed in the observed spectrum. [55] INM approximations to spectroscopy offer only a limited dynamical description, and correspond to an underlying spectral density that is typically broader than the observed lineshape when considering intramolecular modes. As an example, in bulk water (and other liquid state intramolecular lineshapes) INM intramolecular resonances were found to be broader than their TCF counterparts, but with the same central frequency and integrated intensity. Our TCF and INM spectra in Figure 6.3 unambiguously demonstrate SFG O-H stretching lineshapes at the water/vapor interface are significantly motionally narrowed to a degree reminiscent of the bulk. [93, 134] This result also suggests SFG spectra are sensitive to both structure and dynamics. The INM spectrum clearly exhibits the same resonances, but is broader. This implies the observed lineshapes are motionally narrowed, and dynamical contributions to SFG signals are important. [15]

Figure 6.4 presents TCF-derived theoretical descriptions of the SFG spectra in the O-H stretching region for the water/vapor interface. The three possible independent

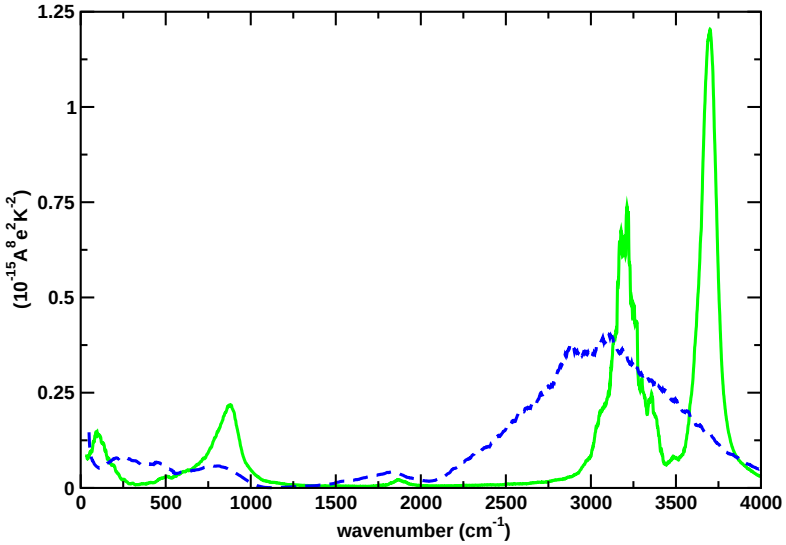

Figure 6.3: SFG TCF and INM Spectra for the Water/Vapor Interface. SFG SSP spectra for the water/vapor interface for the entire water vibrational spectrum using TCF (solid green line) method and INM (dashed blue line) method.

polarization conditions, (SSP, PPP, and SPS), in the electronically nonresonant experiment are displayed. The first two indices can be interpreted as the element of the system polarizability tensor, and the last index as the element of the system dipole that is being probed. In the data, for all polarizations, we have included the SSP nonresonant contribution (this is only strictly correct for the SSP polarization condition, and serves as an estimate in the other cases), $\chi^{NRes}(\omega)$, which is a small negative constant, [5, 140] and the full signal is given by: $|\chi^{(2)}_{SFG}(\omega)|^2 \propto |\chi^{Res}(\omega) + \chi^{NRes}(\omega)|^2$. In order to account for the Fresnel coefficients that modify the experimental intensities, we have adjusted the relative intensities of our theoretical spectra so they can be more easily compared with

experimental results. [15]

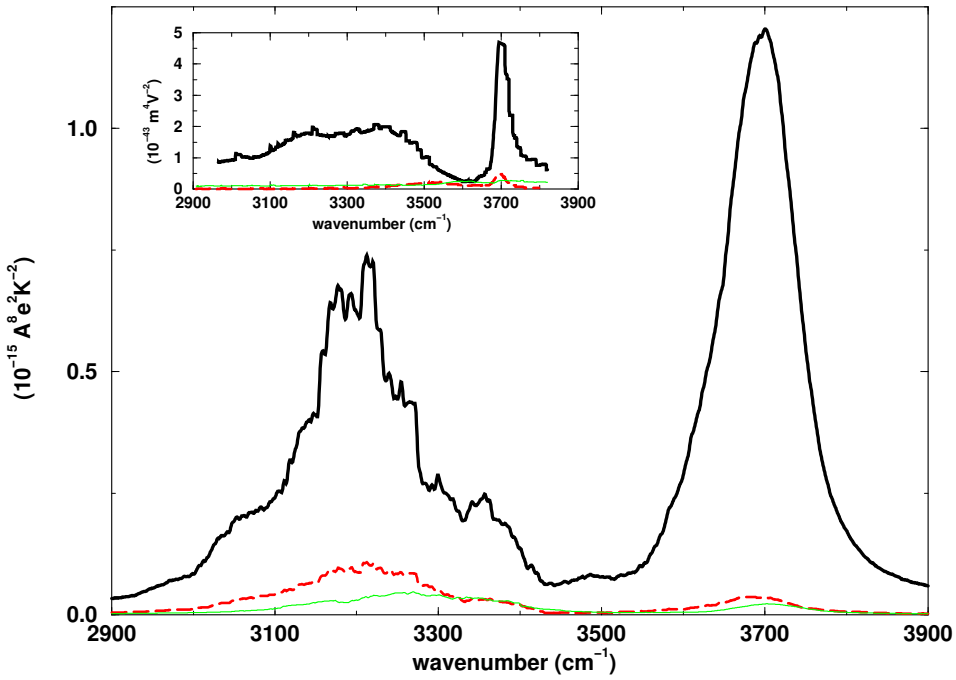

Figure 6.4: SFG TCF Spectra for the O-H Stretching Region. SFG TCF spectra for the water/vapor interface in the O-H stretching region for three polarizations: SSP (solid black line), PPP (dashed red line), and SPS (solid green line). The inset is experimental data [15] for the same polarizations using the same color scheme.

In Figure 6.4, the free O-H peak is prominent at 3700. cm^{-1} and the rest of the O-H stretching region has a more complicated shape. The inset of Figure 6.4 displays experimental data for the O-H stretching region taken in the same polarization geometries. [15] The relative intensities agree nearly quantitatively between theory and experiment. The free O-H stretching lineshape is captured very accurately by the theory and the rest of the O-H region has a similar shape. The ratio of relative intensities between the free O-H and the rest of the OH stretching band are about 2:1 for both experiment and theory.

Clearly the theory captures the essential features of the spectrum and its polarization dependence. To quantitate the polarization dependence, the ratio of the SSP:PPP intensities for the free OH stretch, where the signal to noise is best, is 13:1 (10:1) for the theoretical (experimental) spectra, and the SPS is about a factor of three smaller than the PPP in both cases. The agreement is well within the relative error demonstrating the success of theoretical methods. The agreement between the TCF and experimental spectrum, including the relative intensities of the different polarization conditions, is excellent, and within the statistical error over most of the frequency range. [2]

The spectrum in the SSP geometry that correlates the dipole moment component normal to the interface with diagonal polarizability matrix elements in the plane of the interface ($e.g < \mu_z(0)\alpha_{xx}(t) >$, with the z axis taken as the surface normal direction) leads to the most intense spectrum due to a relatively sizable, and changing, net normal dipole moment at the interface, and the relatively large diagonal polarizability elements; water has a nearly diagonal polarizability matrix with nearly equal elements in both the gas phase and bulk. (Note, the PPP polarization condition is sensitive to a combination of all allowed susceptibility tensor elements in contrast to SSP and SPS that only probe a single tensor element.) [77] Thus, the essential features of the spectrum, and its polarization dependence, are captured very well by the TCF theory with the caveat that absolute intensities of the intramolecular modes are quite sensitive to the choice of polarizability parameters.

The polarization dependence of the signal is demonstrated in Figure 6.4. For polarizations that are sensitive to dipole derivatives normal to the interface – SSP and PPP

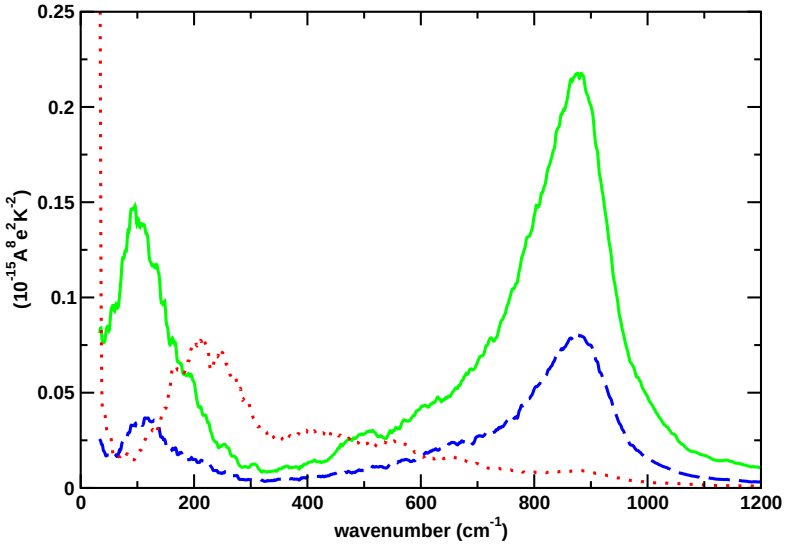

Figure 6.5: SFG TCF Spectra for the Intermolecular Region. SFG TCF spectra for the water/vapor interface in the intermolecular region for three polarizations: SSP (solid green line), PPP (dashed blue line), and SPS (dotted red line).

– the signal has an intense lineshape. In contrast, for the SPS geometry, which is sensitive to dipole derivatives parallel to the interface, only a hint of a signal is found. The SPS polarization condition also probes small off-diagonal polarizability matrix elements. These results also suggest by evaluation of the polarization dependence of the SFG spectra, given a knowledge of the expected nature of the polarizability and dipole derivatives, allows interfacial molecular geometries to be inferred *via* the spectra. [17, 77, 141]

While the intermolecular spectrum of bulk water shows little structure, the interfacial spectra is complex as shown in Figure 6.5. The figure highlights the intermolecular SFG TCF spectra for the three independent polarization conditions, (SSP, PPP and SPS).

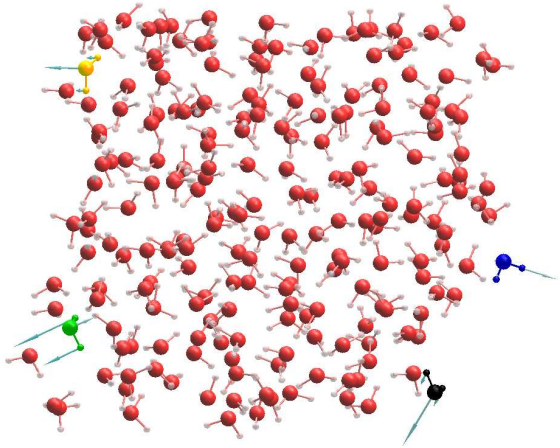

Figure 6.6: Water/Vapor Interface Snapshot. A snapshot of a water/vapor interface containing 216. water molecules featuring INMs from different regions of the spectra. The water molecule shown in blue is representative of a free O-H mode at 3694. cm^{-1}. The water molecule shown in green is representative of a wagging motion at 858. cm^{-1}. The water molecule shown in yellow highlights a translation perpendicular to the interface at 46. cm^{-1}. The water molecule shown in black highlights a translation parallel to the interface at 197. cm^{-1}.

The polarizations that are sensitive to dipole derivatives normal to the interface, SSP and PPP, show a well-defined intermolecular mode at 875. cm^{-1} that is comparable in intensity to the rest of the intermolecular structure and approximately one-sixth the intensity of the intense free O-H stretching peak [2]. Using INM methods (looking at the nature of the INMs in the same spectral region), the resonance is shown to be due to a wagging mode localized on a single water molecule, at a slight angle to the interface,

with two hydrogens vibrating/librating normal to the interface, and the oxygen anchored in the interface. [2] The hydrogens, pointing into the vapor phase, are hydrogen bonded to an oxygen atom at the interface.

The SSP and PPP also show an intense intermolecular mode at 95. cm^{-1}. Using INM methods the resonance is found to be due to translations perpendicular to the interface. The SPS spectra, which is sensitive to dipole derivatives parallel to the interface, shows an intermolecular mode at 220. cm^{-1}. This mode is a result of translations parallel to the interface. The importance of polarization sensitivity in SFG experiments is, thus, highlighted. Further, we have observed spectroscopically distinct species, and clearly identified the vibrational modes responsible for the lineshape. Hence, experimental setups that permit taking spectra at relatively low wavelengths could probe these modes as a compliment to the information contained in the free and donor O-H stretching modes. These three distinct populations of water molecules at the interface were previously undescribed – other works have inferred the existence of something like the wagging mode. [8, 43, 44] This might be considered surprising given the large numbers of MD simulations of the water/vapor interface that have been performed previously. This observation highlights the power of calculating spectroscopic observables in assessing interfacial structure and dynamics. Not only can the results be directly compared with experiment, thus validating the MD model, the spectroscopic calculation serves as a filter of the dynamics extracting out the identity of collective coordinates with well-defined frequencies that persist at the interface.

Figure 6.6 highlights the vibrational modes from the intermolecular and intramolec-

ular region of the spectra. A typical free O-H mode, shown in blue, produces the high-frequency feature at 3700. cm^{-1}. It is clear the oxygen atom is anchored in the interface, and the O-H is oscillating freely above the interface. The wagging mode giving rise to the spectral feature at 875. cm^{-1} is displayed in green at the opposite interface. Here, the oxygen atom is anchored in the interface, and the two hydrogens are vibrating into the vapor phase. A representative perpendicular translational mode (with lineshape centered at 95. cm^{-1}) is shown in yellow, and the roughly parallel translational mode (with lineshape centered at 220. cm^{-1}) is shown in black. These results demonstrate how INM approach does not require *a priori* assumptions about the nature of interfacial modes but does reveal their physical characteristics, and how different molecular motions contribute to the spectrum.

Figure 6.7 displays the distribution of the direction cosine from the surface normal of O-H vectors pointing into the vapor. This result compares well with previous theoretical data. [6] We see an enhancement in probability at $\cos\theta \approx 1$. We also find approximately 20.% of surface water molecules have a free O-H bond pointing out of the liquid, and into the vapor which is consistent with previous theoretical [6] and experimental [26] work. This analysis also points out it is necessary to talk of broad distributions of angles at the water/vapor interfaces, and that relatively less can be learned from single average values of orientations.

Figure 6.8a displays the real and imaginary parts for the SSP spectrum calculated via equations 3.11 and 3.12. Examining the real and imaginary parts of the spectrum can offer insights unavailable from the modulus alone. The real and imaginary parts could

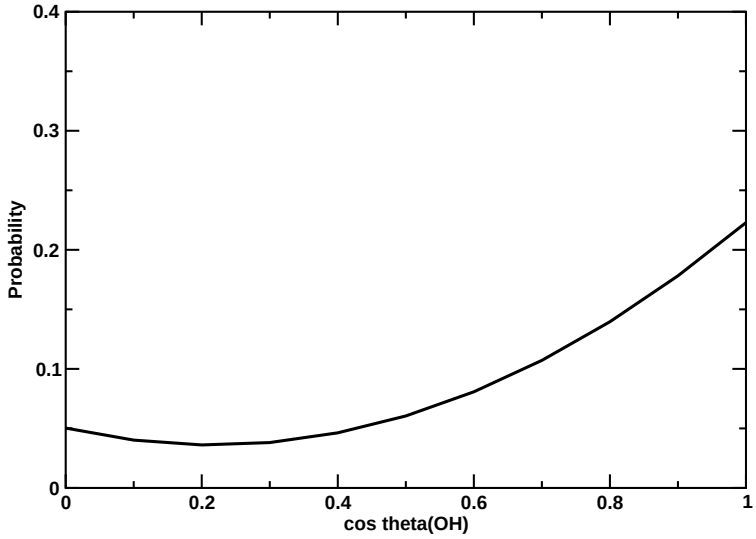

Figure 6.7: Probability Distribution of the Direction Cosine. The probability distribution of the direction cosine from the surface normal of O-H vectors pointing into the vapor.

be measured experimentally *via* a heterodyne detection scheme, or by taking advantage of interference effects between bulk and interfacial contributions to the spectrum. [17] To see the advantages of separately examining the real and imaginary contributions, it is useful to write the resonant SFG signal of a single harmonic mode, Q, (with linear dipole and polarizability) in frequency space as the following: [6]

$$\chi_R^{(2)}(\omega) \propto (\partial\mu_i/\partial Q)\,(\partial\alpha_{jk}/\partial Q)\left[\frac{\omega-\omega_{IR}}{(\omega-\omega_{IR})^2+\gamma^2}\right] \tag{6.1}$$

$$\chi_I^{(2)}(\omega) \propto (\partial\mu_i/\partial Q)\,(\partial\alpha_{jk}/\partial Q)\left[\frac{\gamma}{(\omega-\omega_{IR})^2+\gamma^2}\right] \tag{6.2}$$

In Equations 6.1-6.2, γ is a mathematical convergence parameter that physically can be interpreted as a homogeneous line width. The signal magnitude is seen to be proportional

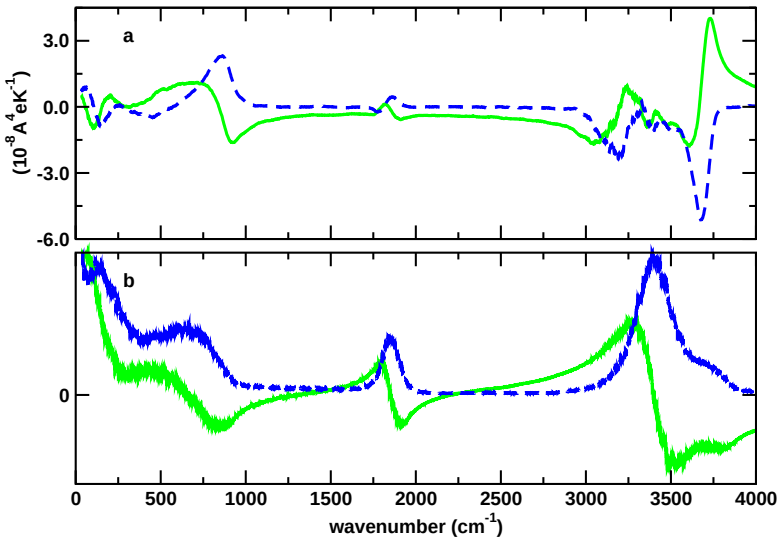

Figure 6.8: Real and Imaginary Components of the Spectra. Real (solid green line) and imaginary (dashed blue line) components of the (a) SFG SSP TCF spectra for the water/vapor interface and for (b) bulk water calculated as the Fourier-Laplace transform.

to the product of dipole and polarizability derivatives. Equations 6.1-6.2 imply a single type of mode will lead to an imaginary contribution that is a symmetric well-defined peak (Lorentzian in character) while the real part will change sign, dipping below zero, at the maximum of the imaginary portion. If more than one species is contributing to the signal in a given region, a more complex lineshape will result from the overlapping signals. Examining the real and imaginary contributions in Figure 6.8a, it is clear several of the resonances are essentially single mode in character: the free O-H (3700. cm^{-1}), the small bending contribution at the surface (1800. cm^{-1}), the wagging mode (875. cm^{-1}), and translational modes (95. cm^{-1} and 220. cm^{-1}). There is some overlap in

the translational modes, and it is instructive the higher frequency 220. cm^{-1} mode, that is pronounced only in the SPS modulus spectrum, also shows up in the SSP real and imaginary spectra.

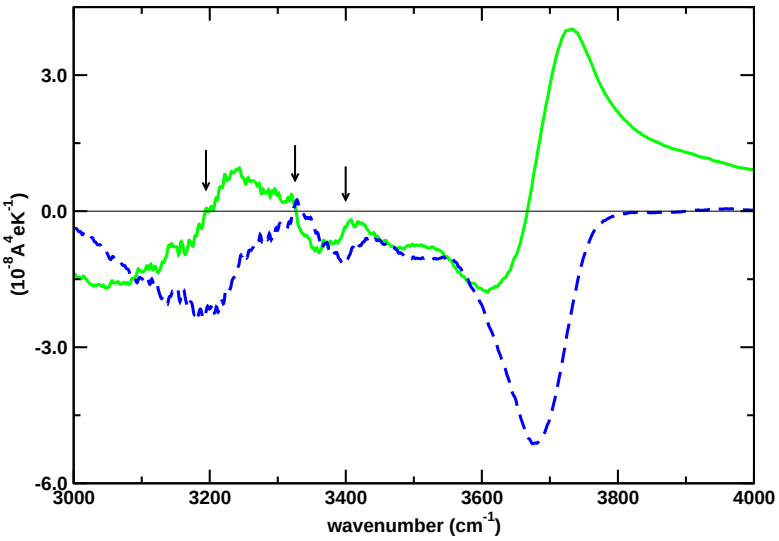

Figure 6.9: Real and Imaginary Components in the O-H Stretching Region. Real (solid green line) and imaginary (dashed blue line) components of the SFG SSP TCF spectra for the water/vapor interface for the O-H stretching region. The arrows highlight three separate modes centered at 3195. cm^{-1}, 3325. cm^{-1}, and 3400. cm^{-1}.

Figure 6.9 highlights the O-H stretching region – from approximately 3000. cm^{-1} to 3600. cm^{-1}. Careful examination of the spectrum reveals three separate modes in this region centered at 3195. cm^{-1}, 3325. cm^{-1}, and 3400. cm^{-1}. Remarkably, this agrees very well with previous experimental work that deconvoluted the spectrum in this region. That analysis revealed three modes present in the same region centered at 3200. cm^{-1},

3310. cm^{-1} and 3420. cm^{-1} – nearly the same frequencies. [20] This is strong evidence for distinct populations of water molecules in this "donor" O-H region of the spectrum. Further work is needed to identify the nature of these distinct O-H stretching species. Note, the theoretical and experimental spectra have a somewhat different shape in this region, and this manifests itself in the relative intensities of the different contributions. The experimental spectrum is more pronounced on the blue side (to the red of the free O-H peak) compared to the theoretical result, and the subpopulations identified on that side of the lineshape are relatively larger as well. This is most likely due to the spectroscopic intensities of these species *via* our spectroscopic model rather than different populations of these species at the interface within the MD model. However, further investigation is required to definitively demonstrate this. It should also be noted, as pointed out in an earlier work, [6] orientational information can also be deduced from the relative signs of the imaginary mode lineshapes given knowledge of the the signs of the prefactors in Equations 6.1-6.2 (the dipole and polarizability derivatives).

To further show the utility of the real and imaginary modal analysis, Figure 6.8b displays the real and imaginary parts of the bulk water O-H stretching region calculated as the Fourier-Laplace transform. While a linear IR experiment does not measure this observable, the transform can still be applied as an analysis tool. Figure 6.8b is strong evidence there are two distinct species in the bulk, and the higher frequency moiety arises from the bulk free O-H, non-hydrogen bonded molecules. [138, 139, 142]

Chapter 7

Conclusion

SFG experimental measurements are growing in number and importance; they are providing valuable information about interfacial structure and dynamics that would be difficult to measure, or are not obtainable otherwise. Theoretical studies are only now sufficiently sophisticated that they can begin to play the major role simulation has in modeling and interpreting condensed phase spectroscopy. In principle, SFG spectroscopy is capable of giving a complete picture of the interface – including structure and dynamics. Realizing this promise depends critically on the spectra being reliably interpreted, and the methods described here are capable of unambiguously characterizing the nature of SFG spectra – including inferring subpopulations of molecules from complex lineshapes. Still, a vigorous interplay between theory and experiment is needed to further develop the interpretative and predictive power of theoretical studies. The investigation of more complex interfaces using the improved TCF methods, described here, will help to both interpret the large and growing body of experimental data, and to predict heretofore unexplored interfacial vibrational structure. Further, experimental advances are likely to extend the frequency range for SFG measurements into the far IR where theory predicts important interfacial

species are present. Lastly, theoretical and experimental measurements of both the real and imaginary parts of the SFG signal (as opposed to measuring the squared modulus as in the typical homodyne detected experiment) show great promise in helping unravel complex SFG lineshapes.

References

[1] A. Perry, H. Ahlborn, P. Moore, and B. Space, J. Chem. Phys. **118**, 8411 (2003).

[2] A. Perry, C. Neipert, C. Ridley, and B. Space, Phys. Rev. E **71**, 050601(1) (2005).

[3] A. Perry *et al.*, A Theoretical Description of the Polarization Dependence of the Sum Frequency Generation Spectroscopy of the Water/Vapor Interface, submitted to J. Chem. Phys.

[4] A. Perry, C. Neipert, P. Moore, and B. Space, Theoretical Modeling of Interface Specific Vibrational Spectroscopy: Methods and Applications, submitted to Chem. Rev.

[5] A. Morita and J. T. Hynes, J. Phys. Chem.B. **106**, 673 (2002).

[6] A. Morita and J. T. Hynes, Chem. Phys. **258**, 371 (2000).

[7] V. Pouthier, P. Hoang, and C. Girardet, J. Chem. Phys. **110**, 6963 (1999).

[8] I. W. Kuo and C. J. Mundy, Science **303**, 658 (2004).

[9] P. Vassilev *et al.*, J. Chem. Phys. **115**, 9815 (2001).

[10] I. Benjamin, Phys. Rev. Let. **73**, 2083 (1994).

[11] R. S. Taylor, L. X. Dang, and B. C. Garrett, J. Phys. Chem. **100**, 11720 (1996).

[12] E. C. Brown, M. Mucha, P. Jungwirth, and D. J. Tobias, J. Phys. Chem. B **109**, 7934 (2005).

[13] M. G. Brown, D. S. Walker, E. A. Raymond, and G. L. Richmond, J. Phys. Chem. B. **107**, 237 (2003).

[14] A. Morita, Chem. Phys. Lett. **398**, 361 (2004).

[15] X. Wei and Y. R. Shen, Phys. Rev. Lett. **86**, 4799 (2001).

[16] V. Pouthier, C. Ramseyer, and C. Girardet, J. Chem. Phys. **108**, 6502 (1998).

[17] V. Ostroverkhov, G. A. Waychunas, and Y. R. Shen, Phys. Rev. Lett. **94**, 0461021 (2005).

[18] D. K. Hore, M. Y. Hamamoto, and G. Richmond, J. Chem. Phys. **121**, 12589 (2004).

[19] M. Mucha *et al.*, J. Phys. Chem. B **109**, 7617 (2005).

[20] E. A. Raymond, T. L. Tarbuck, and G. L. Richmond, J. Phys. Chem. B. **106**, 2817 (2002).

[21] Y. Shen, Sol. St. Comm. **108**, 399 (1998).

[22] G. Richmond, Ann. Rev. Phys. Chem. **52**, 357 (2001).

[23] G. Richmond, Chem. Rev. **102**, 2693 (2002).

[24] D. E. Gragson and G. L. Richmond, J. Phys. Chem. B. **102**, 569 (1998).

[25] Y. Shen, *Principles of Nonlinear Optics* (Wiley, New York, 1984).

[26] Q. Du, R. Superfine, E. Freysz, and Y. Shen, Phys. Rev. Lett. **70**, 2313 (1993).

[27] C. Raduge, V. Pflumio, and Y. Shen, Chem. Phys. Lett. **274**, 140 (1997).

[28] Y. R. Shen, Proc. Natl. Acad. Sci. U.S.A. **93**, 12104 (1996).

[29] E. Freysz, Q. Du, and Y. R. Shen, Annales de Physique **19**, 95 (1994).

[30] Q. Du, E. Freysz, and Y. Shen, Science **264**, 826 (1994).

[31] R. Superfine, J. Y. Huang, and Y. R. Shen, Phys. Rev. Lett. **66**, 1066 (1991).

[32] D. Gragson and G. Richmond, J. Chem. Phys. **107**, 9687 (1997).

[33] M. G. Brown *et al.*, J. Phys. Chem. A **104**, 10220 (2000).

[34] D. E. Gragson and G. L. Richmond, J. Phys. Chem. B. **102**, 3847 (1998).

[35] D. E. Gragson and G. L. Richmond, J. Am. Chem. Soc. **120**, 366 (1998).

[36] L. F. Scatena, M. G. Brown, and G. L. Richmond, Science **292**, 908 (2001).

[37] S. Baldelli, C. Schnitzer, M. J. Shultz, and D. J. Campbell, J. Phys. Chem. B **101**, 10435 (1997).

[38] S. Baldelli, C. Schnitzer, M. J. Shultz, and D. J. Campbell, Chem. Phys. Lett. **287**, 143 (1998).

[39] M. J. Shultz, C. Schnitzer, D. Simonelli, and S. Baldelli, Int. Rev. Phys. Chem. **19**, 123 (2000).

[40] C. Schnitzer, S. Baldelli, and M. Shultz, J. Phys. Chem. B **104**, 585 (2000).

[41] D. Zhang, J. Gutow, and K. Eisenthal, J. Phys. Chem. **98**, 13729 (1994).

[42] D. Zhang, J. Gutow, and K. B. Eisenthal, J. Chem. Soc. Faraday **92**, 539 (1996).

[43] K. R. Wilson *et al.*, J. Phys. Cond. Matter **14**, L221 (2002).

[44] K. R. Wilson *et al.*, J. Chem. Phys. **117**, 7738 (2002).

[45] H. Held, A. I. Lvovsky, X. Wei, and Y. R. Shen, Phys. Rev. B **66**, 2051101 (2002).

[46] X. Wei *et al.*, J. Phys. Chem. B **104**, 3349 (2000).

[47] M. Bonn, H. Ueba, and M. Wolf, J. Phys. Condens. Matter **17**, S201 (2005).

[48] A. N. Bordenyuk and A. V. Benderskii, J. Chem. Phys. **122**, 134713(1) (2005).

[49] S. Roke, A. W. Kleyn, and M. Bonn, Chem. Phys. Lett. **370**, 227 (2003).

[50] A. Voges *et al.*, J. Phys. Chem B **108**, 18675 (2004).

[51] P. Guyot-Sionnest, W. Chen, and Y. Shen, Phys. Rev. B **33**, 8254 (1986).

[52] E. L. Hommel *et al.*, J. Phys. Chem. B. **109**, 811 (2005).

[53] D. Hore *et al.*, Applied Spectroscopy **58**, 1377 (2004).

[54] C. Schnitzer *et al.*, J. Phys. Chem. A **103**, 6383 (1999).

[55] R. Kubo, in *Fluctuation, Relaxation and Resonance in Magnetic Systems*, edited by D. T. Haar (Oliver and Boyd, Edinburgh and London, 1961).

[56] S. Mukamel, *Principles of Nonlinear Optical Spectroscopy* (Oxford University Press, Oxford, 1995).

[57] H. Ueba, Progr. Surf. Sci. **55**, 115 (1997).

[58] R. W. Boyd, *Nonlinear Optics* (Academic Press, London, 2003).

[59] M. Hayashi, S. H. Lin, and Y. R. Shen, J. Phys. Chem. A **208**, 8058 (2004).

[60] N. Bloembergen and P. Pershan, Phys. Rev. **128**, 606 (1962).

[61] R. Venkatramani and S. Mukamel, J. Phys. Chem. B **109**, 8132 (2005).

[62] A. Tadjeddine *et al.*, Phys. Stat. Sol. (a) **175**, 89 (1999).

[63] F. Vidal and A. Tadjeddine, Rep. Prog. Phys. **68**, 1095 (2005).

[64] A. Tadjeddine and A. Le Rille, Electrochimica Acta **45**, 601 (1999).

[65] R. Silbey, J. Koedijk, and S. Völker, J. Chem. Phys. **105**, 901 (1996).

[66] S. Mukamel, *Principles of Nonlinear Optical Spectroscopy* (Oxford University Press, Oxford, 1995, See Chapter 5 specifically pps. 129-130).

[67] J. B. Asbury *et al.*, J. Phys. Chem A. **108**, 1107 (2004).

[68] A. Bonvalet *et al.*, Phys. Rev. Lett. **76**, 4392 (1996).

[69] X. Wei, P. B. Miranda, C. Zhang, and Y. R. Shen, Phys. Rev. B **66**, 085401(1) (2002).

[70] P. Butcher and D. Cotter, *The Elements of Nonlinear Optics* (Cambridge University Press, Cambridge, 1990).

[71] S. Mukamel and D. Abramavicius, Chem. Rev. **104**, 2073 (2004).

[72] M. Khalil, N. Demirdoven, and A. Tokmakoff, J. Phys. Chem. A **107**, 5258 (2003).

[73] K. Park and M. Cho, J. Chem. Phys. **109**, 10559 (1998).

[74] Y. R. Shen, Annu. Rev. Phys. Chem. **40**, 327 (1989).

[75] T. F. Heinz, in *Nonlinear Surface Electromagnetic Phenomena*, edited by I. Ponath and G. Stegeman (Elsevier, Amsterdam, 1991).

[76] G. A. R. T. F. Heinz, in *Photonic Probes of Surfaces*, edited by I. Ponath and G. Stegeman (Elsevier, Amsterdam, 1995).

[77] X. Zhuang, P. B. Miranda, D. Kim, and Y. R. Shen, Phys. Rev. B. **59**, 12632 (1999).

[78] R. Byer, in *Nonlinear Optics*, edited by P. Harper and B. Wherritt (Academic Press, London, 1977).

[79] E. Sauter, *Nonlinear Optics* (Wiley Interscience, New York, 1996).

[80] Y. L. Yeh *et al.*, J. Chem. Phys. **114**, 1837 (2001).

[81] R. Lu *et al.*, J. Phys. Chem. B **108**, 7297 (2004).

[82] J. Wang, C. Chen, S. Buck, and Z. Chen, J. Phys. Chem. B **105**, 12118 (2001).

[83] P. Guyot-Sionnest and Y. Shen, Phys. Rev. B **38**, 7985 (1988).

[84] K. J. Schweighofer, U. Essmann, and M. Berkowitz, J. Phys. Chem. B. **101**, 3793 (1997).

[85] H. Dominguez, A. M. Smondyrev, and M. L. Berkowitz, J. Phys. Chem. B. **103**, 9582 (1999).

[86] T.-M. Chang and L. X. Dang, J. Chem. Phys. **104**, 6772 (1996).

[87] J. Ducuing, in *Nonlinear Optics*, edited by P. Harper and B. Wherritt (Academic Press, London, 1977).

[88] W. Heitler, *The Quantum Theory of Radiation* (Dover Publications Inc., New York, 1984).

[89] D. A. McQuarrie, *Statistical Mechanics* (Harper and Row, New York, 1976).

[90] R. G. Gordon, in *Advances in Magnetic Resonance*, edited by J. S. Waugh (Academic Press, New York and London, 1968).

[91] R. Kubo, in *Lectures in Theoretical Physics*, edited by W. Britton and L. Dunham (Interscience Publishers Inc., New York, 1959).

[92] B. J. Berne and G. D. Harp, Adv. Chem. Phys. **17**, 63 (1970).

[93] H. Ahlborn, X. Ji, B. Space, and P. B. Moore, J. Chem. Phys. **111**, 10622 (1999), see discussion and references within.

[94] P. Moore, H. Ahlborn, and B. Space, in *Liquid Dynamics Experiment, Simulation and Theory*, edited by M. D. Fayer. and J. T. Fourkas (ACS Symposium Series, New York, 2002).

[95] J. Borysow, M. Moraldi, and L. Frommhold, Mol. Phys. **56**, 913 (1985).

[96] P. A. Egelstaff, Adv. Phys. **11**, 203 (1962).

[97] H. Kim and P. J. Rossky, J. Phys. Chem. B **106**, 8240 (2002).

[98] R. Braun *et al.*, J. Chem. Phys. **110**, 4634 (1999).

[99] Z. Chen, Private communication, 2005.

[100] D. Chandler, *Introduction to Modern Statistical Mechanics* (Oxford University Press, New York, 1987).

[101] B. J. Berne and R. Pecora, *Dynamic Light Scattering* (Robert E. Kroeger Publishing Company, Malabar, Florida, 1990), p. 149.

[102] In our previous paper (Ref. 1) we accidentally showed the harmonic quantum correction factor appropriate for the whole correlation function $C(\omega) = C_{Cl}(\omega)(\beta\hbar\omega/(1-e^{-\beta\hbar\omega})$ instead of the correction for the real part, $C_R(\omega)$, given here. Note that in the high-frequency limit the two factors differ only by a factor of two.

[103] M. P. Allen and D. J. Tildesley, *Computer Simulation of Liquids* (Clarendon Press, Oxford, 1989).

[104] T. Keyes, J. Chem. Phys **104**, 9349 (1996).

[105] W.-X. Li and T. Keyes, J. Chem. Phys. **111**, 5503 (1999).

[106] J. Jang and R. M. Stratt, J. Chem. Phys. **112**, 7524 (2000).

[107] R. E. Larsen and R. M. Stratt, J. Chem. Phys. **110**, 1036 (1999).

[108] R. L. Murry, J. T. Fourkas, W.-X. Li, and T. Keyes, Phys. Rev. Lett. **83**, 3550 (1999).

[109] T. Keyes, J. Phys. Chem. **101**, 2921 (1997).

[110] R. M. Stratt, Acc. Chem. Res. **28**, 201 (1995).

[111] J. Adams and R. Stratt, J. Chem. Phys. **93**, 1632 (1990).

[112] B. Ladanyi and R. Stratt, J. Chem. Phys. **99**, 2502 (1995).

[113] P. Moore and T. Keyes, J. Chem. Phys **100**, 6709 (1994).

[114] P. Moore, A. Tokmakoff, T. Keyes, and M. Fayer, J. Chem. Phys **103**, 3325 (1995).

[115] X. Ji *et al.*, J. Chem. Phys. **113**, 8693 (2000).

[116] H. Ahlborn, X. Ji, B. Space, and P. B. Moore, J. Chem. Phys. **112**, 8083 (2000).

[117] X. Ji *et al.*, J. Chem. Phys. **112**, 4186 (2000).

[118] H. Ahlborn, X. Ji, B. Space, and P. B. Moore, J. Chem. Phys. **111**, 10622 (1999).

[119] P. B. Moore, X. Ji, H. Ahlborn, and B. Space, Chem. Phys. Lett. **296**, 259 (1998).

[120] M. Ribeiro, M. Wilson, and P. Madden, J. Chem. Phys. **110**, 4803 (1999).

[121] X. Ji *et al.*, J. Chem. Phys. **112**, 4186 (2000).

[122] P. Moore and B. Space, J. Chem. Phys. **107**, 5635 (1997).

[123] E. F. David and R. Stratt, J. Chem. Phys. **109**, 1375 (1998).

[124] B. Space, H. Rabitz, A. Lőrincz, and P. Moore, J. Chem. Phys. **105**, 9515 (1996).

[125] T. Keyes, J. Chem. Phys **106**, 46 (1997).

[126] J. R. Reimers and R. O. Watts, Chem. Phys. **91**, 201 (1984).

[127] M. Cho *et al.*, J. Chem. Phys. **100**, 6672 (1994).

[128] J. Applequist, J. R. Carl, and K.-K. Fung, J. Am. Chem. Soc. **94**, 2952 (1972).

[129] J. Applequist and C. O. Quicksall, J. Chem. Phys. **66**, 3455 (1977).

[130] J. R. Partington, *An Advanced Treatise on Physical Chemistry, Vol. 4* (Longmans, Green and Co., London, 1953).

[131] L. Silberstein, Philos. Mag. **33**, 521 (1917).

[132] R. DeVane, C. Ridley, T. Keyes, and B. Space, J. Chem. Phys. **119**, 6073 (2003).

[133] R. DeVane *et al.*, J. Chem. Phys. **121**, 3688 (2004).

[134] C. P. Lawrence and J. L. Skinner, J. Chem. Phys. **117**, 5827 (2002).

[135] M. Tuckerman, B. J. Berne, and G. J. Martyna, J. Chem. Phys. **97**, 1990 (1992).

[136] K. A. Bode and J. Applequist, J. Phys. Chem. **100**, 17820 (1996).

[137] M. Souaille and J. C. Smith, Mol. Phys. **87**, 1333 (1996).

[138] C. P. Lawrence and J. L. Skinner, J. Chem. Phys. **117**, 8847 (2002).

[139] C. P. Lawrence and J. L. Skinner, J. Chem. Phys. **118**, 264 (2003).

[140] E. A. Raymond and G. L. Richmond, J. Phys. Chem. B **108**, 5051 (2004).

[141] J. Wang, Z. Paszti, M. A. Even, and Z. Chen, J. Am. Chem. Soc. **124**, 7016 (2002).

[142] K. B. Moller, R. Rey, and J. T. Hynes, J. Phys. Chem. A **108**, 1275 (2004).

About the Author

Angela S. Perry received a Bachelor's of Arts Degree from the University of South Florida in May of 2000. She entered the Doctoral program at the University of South Florida in the Fall of 2000. She began work in computational chemistry with Professor Brian Space in December of 2000.

In addition to graduate coursework, Ms. Perry attended the Gordon-Kenan Chemical Physics Summer School, held at Roger Williams University. She has also attended several Gordon Research Conferences and American Chemical Society National Meetings. As the graduate student representative in 2002, Ms. Perry was the Chair for the Castle Student Research Conference at USF.

While in the Ph.D. program at the University of South Florida, Ms. Perry was a recipient of the George Bursa Doctoral Fellowship Award. She was awarded two summer awards from the Tharp Endowed Scholarship Fund and three travel awards from the Gordon Conference Chair's Fund. She has coauthored five publications and made several presentations at regional and national meetings.